

Analysis of the Busemann Biplane Characteristics Using MATLAB and ANSYS Simulations

a project presented to
The Faculty of the Department of Aerospace Engineering
San José State University

in partial fulfillment of the requirements for the degree
Master of Science in Aerospace Engineering

by

Aaron B. Eckert

December 2021

approved by

Dr. Periklis Papadopoulos
Faculty Advisor



©2021

Aaron B. Eckert

ALL RIGHTS RESERVED

ABSTRACT

Analysis of the Busemann Biplane Characteristics using MATLAB and ANSYS Simulations

Aaron B. Eckert

The potential exists to optimize the concept of a supersonic biplane by varying numerous design parameters at once. This project investigates the impacts of employing design optimization across multiple design variables. The focus is on reducing wave drag by mitigating flow choking at off-design conditions, thereby positively affecting the aerodynamic coefficients. The optimization schemes employ a larger design space than have been utilized in recent years. Additional design considerations include relative position, wedge angles and chord lengths. A general inviscid model was built in MATLAB. This was used to refine the design space by eliminating designs in which subsonic flow occurred. The reduced design space was fed into the ANSYS Design Exploration Direct Optimization application. The design optimization was run for multiple design parameters. Design candidate points are listed within the report. A key finding was that the complex nature of the shock wave interactions dramatically affects the lift and drag coefficients for a Busemann-type biplane.

ACKNOWLEDGEMENTS

First and foremost, I would like to thank my advisor Dr. Papadopoulos for his guidance and support during this project, as well as my six years at San Jose State University. I'd like to acknowledge Dr. Mourtos for encouraging me to continue my education. I also appreciate the classmates I've worked with because we've challenged each other and developed our intuitive understanding of complicated topics. Finally, I wouldn't have made it this far had it not been for my mom, dad and Týra.

TABLE OF CONTENTS

ABSTRACT	iii
ACKNOWLEDGEMENTS	iv
LIST OF TABLES	vii
LIST OF FIGURES	viii
NOMENCLATURE	x
Chapter 1 – Introduction	1
1.1 Motivation	1
1.2 Literature Review	2
1.2.1 Minor 2-D Modifications.....	2
1.2.1.1 Relative angle and size.....	2
1.2.1.2 Relative Position	4
1.2.2 Major 2-D Modifications.....	7
1.2.2.1 High Lift Devices (HLD).....	7
1.2.2.2 Shape optimizations	10
1.2.3 3-D Considerations	15
1.2.4 Historical Data Comparison	18
1.3 Project Proposal.....	20
Chapter 2 – Background	22
2.1 Overview of Supersonics	22
2.1.1 Bow Shocks Shock Waves	22
2.1.2 Shock Expansion Theory	23
2.1.3 The Method of Characteristics	25
2.1.4 Aerodynamic Forces.....	25
2.1.4.1 Lift.....	26
2.1.4.2 Drag.....	26
2.1.4.3 Friction Drag.....	26
2.1.4.4 Wave Drag	27
2.2 Overview of the Busemann Biplane.....	27
2.2.1 Design logic	27
2.2.2 Flow Choking and Hysteresis.....	28
Chapter 3 – Theoretical Approach	29
3.1 Body Definition.....	29

3.2 Initial Wave Construction	30
3.3 Fore Section Shock Interactions.....	31
3.4 Aft-section Shock-Expansion Interaction	33
3.5 Theoretical Flow Values and Coefficients	35
3.6 Limitations	35
3.6.1 Limitations Within Shock-Expansion Theory	35
3.6.2 Limitations Within the Coding Methodology	36
Chapter 4 – Computational Approach	37
4.1 Computational Domain Definition.....	37
4.2 Grid Generation.....	38
4.3 Fluent Settings.....	39
4.4 Grid Independence and Verification Against Historical Data	40
Chapter 5 - Verification and Validation	43
5.1 Verification Against Historical Data.....	43
5.1.1 Verification of Preliminary Wave Calculation.....	43
5.2 Baseline Benchmark Studies Between Theory and CFD.....	44
5.2.1 Baseline Benchmark Study Between Theory and CFD for Viscous Models	45
5.2.2 Benchmark Study of the fanDensity Variable	51
Chapter 6 – Optimization of Supersonic Biplane	55
6.1 Exploration of the Design Space using MATLAB	55
6.1.1 Symmetric Body Angles with Varied Vertical and Horizontal Offsets	55
6.1.2 Symmetric Body Angles with Varied Chord Lengths.....	58
6.1.3 Asymmetric Body Angles, Fully Random Chord Lengths and Offsets	60
6.2 ANSYS Direct Optimization.....	61
6.2.1 Symmetric Body Angles with Varied Vertical Offset.....	62
6.2.2 Symmetric Body Angles with Varied Vertical and Horizontal Offsets	62
6.2.3 Asymmetric Body Angles, Fully Random Chord Lengths and Offsets	63
Chapter 7 – Conclusion	65
7.1 Future Work	65
References	66

LIST OF TABLES

Table 2. 1 – Characteristics definition	25
Table 3. 1 – Design variables.....	29
Table 3. 2 – Surface definitions	30
Table 3. 3 – Flow vector definitions	31
Table 3. 4 – Waves structured array variable definitions	33
Table 5. 1 - Baseline 1 and 2 value comparison	45
Table 5. 2 - Baseline 1, Mach 1.7, lift & drag coefficient	47
Table 5. 3 – Baseline 1, Mach 1.7, breakdown of surfaces	47
Table 5. 4 – Baseline 1, Mach 2, lift & drag coefficient.....	48
Table 5. 5 – Baseline 1, Mach 2, breakdown of surfaces	48
Table 5. 6 – Baseline 2, Mach 1.7, lift & drag coefficient.....	50
Table 5. 7 – Baseline 2, Mach 1.7, breakdown of surfaces	50
Table 5. 8 – Baseline 2, Mach 2, lift & drag coefficient.....	50
Table 5. 9 – Baseline 2, Mach 2, breakdown of surfaces	50
Table 6. 1 – Range of input parameters (VO only).....	62
Table 6. 2 – Design candidate points (VO).....	62
Table 6. 3 – Range of input parameters (VO, HO).....	63
Table 6. 4 - Design candidate points (VO, HO)	63
Table 6. 5 – Range of input parameters – all parameters.....	64
Table 6. 6 - Design candidate points – all parameters	64

LIST OF FIGURES

Figure 1. 1 – Example of graphical calculation method [1]	3
Figure 1. 2 – Effects of increasing the lower edge angles on the lift and drag coefficients of the Busemann biplane at Mach 3.0 [1]	4
Figure 1. 3 - Drag coefficient and L/D variation for staggered configurations	5
Figure 1. 4 - Drag coefficient of continuous staggered configuration in inviscid flow	6
Figure 1. 5 - Drag coefficient of continuous staggered configuration in viscous flow	6
Figure 1. 6 - Lift and drag coefficients through simulated take-off to cruise conditions	7
Figure 1. 7 - Drag coefficient comparison of leading edge deflected flap configuration compared against baselines.....	8
Figure 1. 8 - Drag coefficient comparison of trailing edge deflected flap configuration compared against baselines.....	9
Figure 1. 9 - Drag coefficient comparison of configuration with both flaps deflected compared against baselines.....	9
Figure 1. 10 - Flow chart showing inverse design methodology	10
Figure 1. 11 - Cross-sectional diagram of the design biplane surfaces	11
Figure 1. 12 - Pressure coefficient of the designed biplane compared against the intended results	11
Figure 1. 13 - Cross section of proposed new supersonic biplane.....	12
Figure 1. 14 - Cross-section of the generated symmetrical biplane airfoil compared (blue) against the baseline (red).....	13
Figure 1. 15 - Comparison of drag coefficient across flight Mach numbers for symmetric generated biplane against baselines	14
Figure 1. 16 - Cross-sectional comparison of the generated asymmetrical biplane (blue) against the baseline (red).....	14
Figure 1. 17 - Comparison of drag coefficient across flight Mach numbers for asymmetric generated biplane against baselines	15
Figure 1. 18 - Drag coefficient comparison of rectangular wing platform and tapered wing platform.....	16
Figure 1. 19 - Drag coefficient comparison of sweep cases	16
Figure 1. 20 - Drag comparison of box winglet vs open biplane configurations	17
Figure 1. 21 - Cross sectional depiction of applied aerodynamic taper. Lift to drag ratio and lift coefficient along the wingspan of the results of the inverse design method	18
Figure 1. 22 – Comparison of the inviscid vs viscous laminar drag coefficients of historical data	19
Figure 1. 23 – Comparison of hysteresis regions compared to baseline.....	20
Figure 2. 1 - Pressure coefficient contours during acceleration.....	23
Figure 2. 2 - Flat plate at an angle of attack [10].....	26
Figure 2. 3 - Busemann biplane at angle of attack [1]	27
Figure 3. 1 – Example of a randomly generated supersonic biplane	30
Figure 3. 2 – Example of fore shock interactions with wave designations.....	32

Figure 3. 3 - Visualization of the flow through the aft section of the biplane	34
Figure 3. 4 - Comparison between predicted theoretical flow field and historical CFD	34
Figure 4. 1 – Farfield employed.....	37
Figure 4. 2 – Symmetrical biplane configuration with dimensions	38
Figure 4. 3 – Asymmetrical biplane configuration with dimensions.....	38
Figure 4. 4 – Near grid around symmetrical biplane set.....	39
Figure 4. 5 – Near grid around asymmetrical biplane set	39
Figure 4. 6 – Pressure contours from ANSYS	40
Figure 4. 7 – Pressure contours from historical data generated in UPACS [5]	41
Figure 4. 8 – Grid independence study	41
Figure 4. 9 – Results from grid independence study	42
Figure 5. 1 – Preliminary wave validation.....	43
Figure 5. 2 – L/D vs AoA validation of initial wave formulation	44
Figure 5. 3 – ANSYS set up.....	45
Figure 5. 4 - MATLAB graphical display for Mach 1.7.....	46
Figure 5. 5 - ANSYS graphical display for Mach 1.7	47
Figure 5. 6 - MATLAB graphical display of baseline 2 at Mach 1	49
Figure 5. 7 - ANSYS graphical display of baseline 2 at Mach 1	49
Figure 5. 8 – Pressure contours of BL2 M1.7 inviscid vs viscous turbulent	51
Figure 5.9 – Drag coefficient & computation time vs fanDensity values, baseline 1, Mach 1.7 .	52
Figure 5. 10 – Drag coefficient and computation time vs fanDensity values, baseline 1, Mach 252	
Figure 5. 11 - Lift coefficient and computation time vs fanDensity values, baseline 2, Mach 1.7	
.....	53
Figure 5. 12 – Drag coefficient and computation time vs fanDensity values, baseline 2, Mach 1.7	
.....	53
Figure 5. 13 – Drag coefficient and computation time vs fanDensity values, baseline 2, Mach 254	
Figure 5. 14 – Lift coefficient and computation time vs fanDensity values baseline 2, Mach 2..	54
Figure 6. 1 - Parallel coordinate plot of symmetric body angles with varying vertical and horizontal offsets.....	56
Figure 6. 2 - Quartile representation of fig. 6.1	56
Figure 6. 3 - 3D scatter plot representation of fig. 6.1	57
Figure 6. 4 - Single and double elimination points from fig. 6.1	57
Figure 6. 5 – Parallel coordinate plot of symmetric body angles with varying chord lengths	58
Figure 6. 6 – Quartile representation of fig. 6.5.....	58
Figure 6. 7 – 3D scatter plot representation of fig. 6.5	59
Figure 6. 8 – Single and double elimination points from fig. 6.5	60
Figure 6. 9 - Parallel coordinate plot of asymmetric body angles with varying vertical and horizontal offsets.....	61
Figure 6. 10 – Quartile representation of fig. 6.9.....	61

NOMENCLATURE

Grouping	Symbol	Definition	Units (SI)
Latin			
	C	Characteristic	
	M	Mach Number	
	P/P	Pressure Ratio	
	T/T	Temperature Ratio	
	lc	Lower chord length	[m]
	uc	Upper chord length	[m]
	LSm	Lower Surface slope	
	USm	Upper Surface slope	
Greek			
	β	Oblique Shock Angle	Degrees
	γ	Specific heat ratio	
	θ	Flow Direction Angle	Degrees
	ρ/ρ	Density ratio	
	ν	Prandtl-Meyer Function	
	μ	Mach Angle	Degrees
Subscripts			
	0	Total	
	1	Upstream of shock/expansion wave	
	2	Downstream of shock/expansion wave	
	n	Normal to shockwave	
	S1	Surface 1	
	S4	Surface 4	
	+	Left running characteristic	
	-	Right running characteristic	
	p	Point in consideration.	

Chapter 1 – Introduction

1.1 Motivation

The first mention of a barrier at the speed of sound occurred in the British publication *Military Science Today* in 1940, just 33 years after the first flight of the Wright Brothers. Seven years later, Chuck Yeager broke the sound barrier for the first time in the Bell X-1 rocket plane, proving that humans could fly faster than the speed of sound. The BAC Concorde was introduced in 1976 as the first commercially available supersonic transport vehicle. It was discontinued in 2003 due to environmental and noise factors. Researchers have been exploring how to make supersonic travel easier, more reliable, safer, faster, and more economical. They are primarily focused, however, on mitigating the noise generated during supersonic flight by way of shock wave reduction or elimination.

Supersonic aircraft often suffer from high drag - specifically wave drag - due to the generation of shock waves over and near the surface of the craft. High drag can dramatically reduce the performance of the craft. Reducing drag will result in improved fuel performance, enhanced flight endurance, as well as the potential to achieve higher speeds. There have been many methods proposed to reduce the drag experienced by crafts flying at supersonic speeds. Additionally, research has been conducted to develop airfoils that have favorable lift to drag ratios at supersonic speeds.

An often-overlooked supersonic airfoil design is the Busemann Biplane first proposed by Adolf Busemann at the Volta Conference in 1935. The Busemann biplane, as the name suggests, employs two lift generating surfaces triangular in cross-section. The peaks of the triangular airfoils face inward and functionally cancel out the shockwaves generated at the tips, substantially reducing wave drag. This promotes favorable shockwave interactions such that the wave-drag can be reduced to nearly zero. Unfortunately, this only occurs at zero lift conditions at and beyond the designed Mach number. Typically, at speeds below the designed Mach number, oblique shocks will form between the surfaces, effectively choking the flow and dramatically increasing drag. Additionally, there exists a flow hysteresis issue wherein favorable shock interactions do not occur until speed is increased to some degree beyond the design mach. It is for these reasons that the Busemann biplane was not actively pursued. In recent years, however, the advent of computational fluid dynamics has allowed researchers to revisit this concept for its potential to generate lift at supersonic speeds without the typically associated sonic boom. These researchers have found impressive results in optimizing the design using modern techniques and show that, potentially, the issues of flow choking, and flow hysteresis may be mitigated or eliminated.

Most of the research conducted has been relatively limited in scope, performing minor surface curvature optimization altering the relative position of the two airfoils, or implementing control surfaces. There is the potential to further optimize the concept of a supersonic biplane by varying numerous design parameters at once. This project investigates the impacts of employing design optimization across multiple design variables.

1.2 Literature Review

1.2.1 Minor 2-D Modifications

1.2.1.1 Relative angle and size

The NACA Technical Report No. 1316 is one of the earliest attempts to optimize the performance of the Busemann biplane by varying design parameters [1]. The investigation focused primarily on the effects of varying the wedge angles of the individual foils while maintaining equal chord lengths for the upper and lower airfoils. The changes in aerodynamic performance were calculated by varying the edge angles individually and in pairs. The aerodynamic coefficients of the biplanes were compared with those of a diamond airfoil as well as a flat plate under the same conditions. The aerodynamic coefficients of a biplane consisting of an upper airfoil with constant wedge angles of 7° and a lower airfoil with constant wedge angles of 10° were calculated between Mach 2.1 and 3.6. Additionally, the variation of the center of pressure with angle of attack as well as the relative loading of the airfoils were calculated and displayed in figure 8 on page 27 of reference [1].

Flow field variables were calculated using Prandtl-Meyer Expansion Theory for pressure changes, in conjunction with Oblique-Shock Theory for the changes in flow direction. For ease of calculation, the change in pressure across the shock waves was calculated utilizing Prandtl-Meyer Relations, with the assumption that the shock waves were weak enough to be approximately isentropic. This approximation created considerable error in the calculated flow direction downstream of the shockwaves. To mitigate this, oblique-shock relations were used to calculate downstream flow direction, while the Prandtl-Meyer relations were used to calculate pressure coefficients downstream of the leading-edge shock waves. The expansion waves were approximated as a series of Mach waves rather than a continuous region, and expansion wave interactions were assumed to occur instantaneously. Aerodynamic coefficients were calculated by integration of the pressure distribution around the biplane surfaces.

Moeckel divided the calculations into two categories: variable spacing biplanes -- those where the shockwaves generated by the leading edges are eliminated by impinging on the interior corners and constant spacing biplanes and -- those where the shockwaves persist through the length of the airfoils. [1] The variable spacing simplified calculations, allowing for the use of early computing machines to process the pressure integrals and derive the aerodynamic coefficients. The flow field became too complex for their computational methods when the shockwaves generated by the leading edges were not eliminated by the interior corners. For these conditions, flow field variables and aerodynamic coefficients were calculated by hand using a graphical approach. An example of the graphical approach taken is given below.

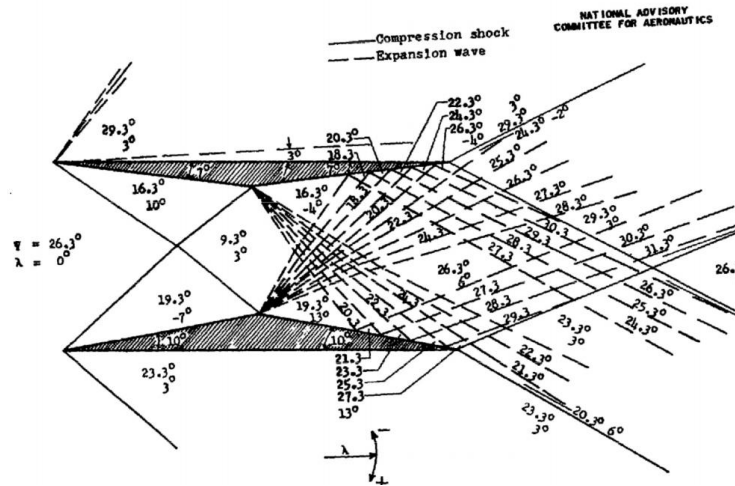


Figure 1. 1 – Example of graphical calculation method [1]

The results gathered through his investigation show consistent shock wave interactions at design conditions where favorable shockwave interactions led to the elimination of interior shock waves. Five key results are listed:

1. For any given lift coefficient, a triangular-section biplane has lower drag than a diamond airfoil of the same thickness ratio.
2. When all edge angles are varied simultaneously, the lift-drag ratio increases as the angles are decreased.
3. With an upper airfoil of constant thickness, the maximum lift-drag ratio obtainable decreases as the thickness of the lower airfoil is increased. For low angles of attack, however, the lift-drag ratio of a biplane may be increased by making the lower airfoil thicker than the upper airfoil. If the lower-edge angles are too greatly increased, an optimum value is passed, and the lift-drag ratio drops.
4. The lift-drag ratio of biplanes may be slightly improved by making the trailing-edge angles somewhat smaller than the leading-edge angles. See figure 1.2 below.
5. The variation of the center of pressure with angle of attack is considerably greater for unsymmetrical than for symmetrical biplanes.

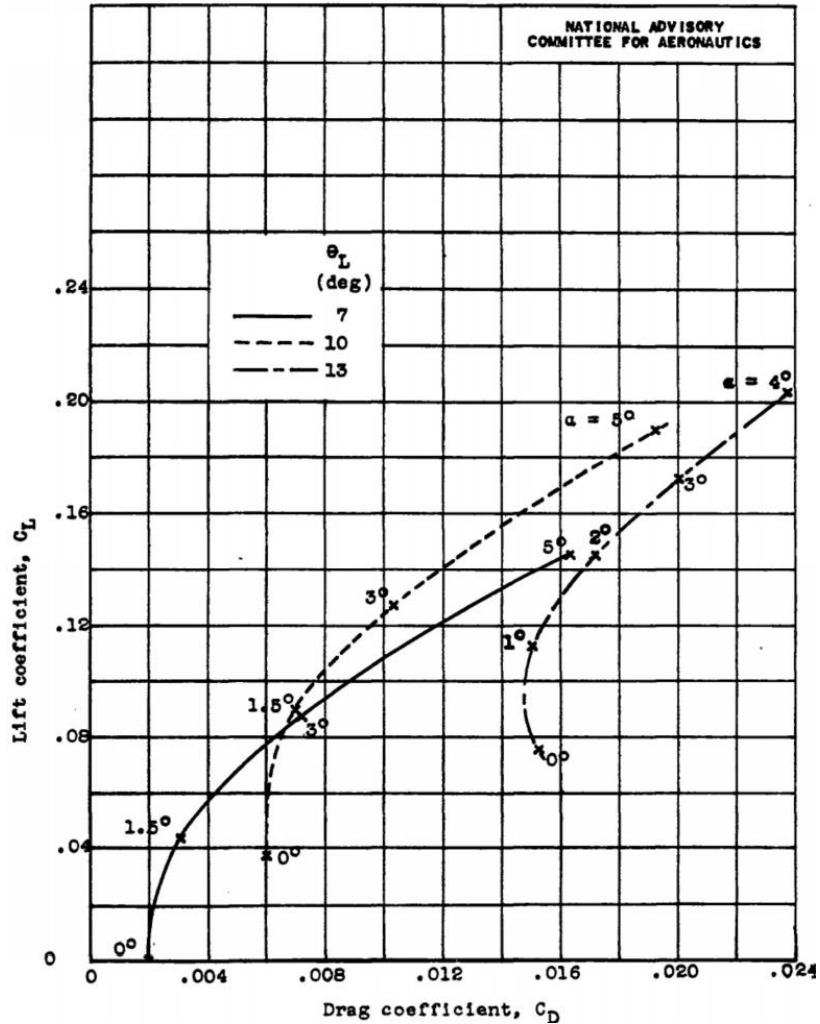


Figure 1.2 – Effects of increasing the lower edge angles on the lift and drag coefficients of the Busemann biplane at Mach 3.0 [1]

1.2.1.2 Relative Position

Two recent papers examined the effects of staggering airfoil configurations of the Busemann biplane for the purposes of mitigating the choking phenomena. The first paper reviewed was *Numerical Investigation of the Effect of Stagger on the Aerodynamic Characteristics of a Busemann Biplane* [2]. It was written by Vijay Kumar Patidar, Rajesh Yadav, and Sudhir Joshi from the Department of Aerospace Engineering, University of Petroleum & Energy Studies in India in 2016, and published by Elsevier. ANSYS Fluent was utilized to simulate supersonic flow over the biplane at various configurations. A structured mesh was employed. The variation in viscosity was modeled using the Sutherland Formula. Turbulence was simulated using the Spalart-Almaras Turbulence Model. Various staggered configurations were studied by shifting the lower airfoil longitudinally back by half a chord length at 0.1 c intervals.

The results of their investigation indicated that longitudinal stagger showed promise as a method to mitigate the choking phenomena without substantially affecting the wave cancellation. Their simulations showed that the choking phenomena for a biplane in Mach 1.6 flow can be mitigated by a stagger of 0.2 c or more. See figure 1.3 below.

A reduced drag was observed at all Mach numbers; however, it was not completely eliminated in the transonic region. At low angles of attack, the staggered configurations consistently improved lift to drag ratio and aerodynamic efficiency in the subsonic and transonic ranges. However, at supersonic speeds, the staggered configurations were shown to increase drag over the standard configuration. The researchers made the comparison between the Busemann biplane and the de Laval nozzle and concluded that the staggered configurations increase the throat area which reduces the choking characteristics without affecting the wave cancellation. [2].

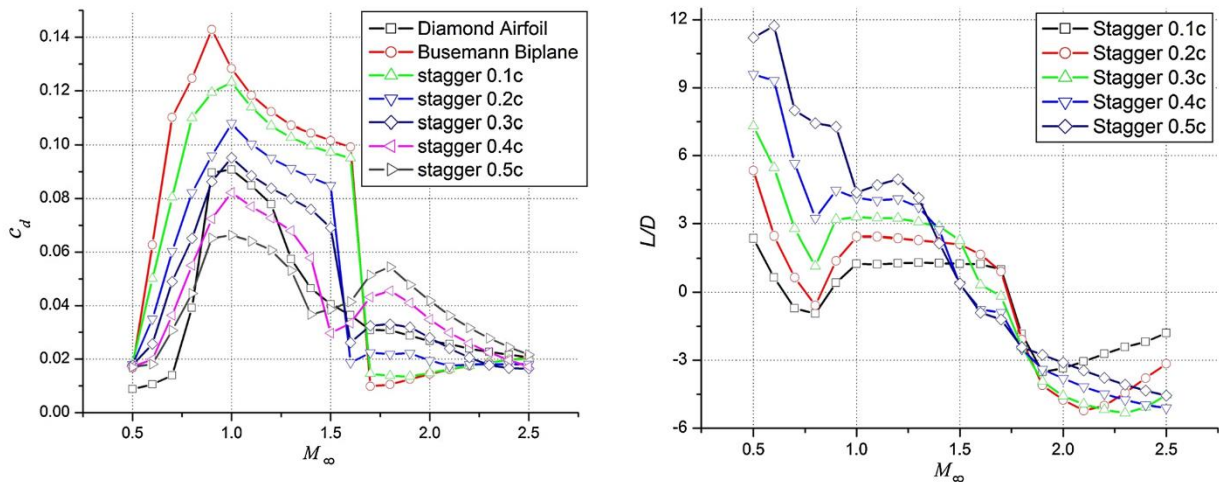


Figure 1. 3 - Drag coefficient and L/D variation for staggered configurations

In 2020, working off of this research, Boping Ma, Gang Wang, Jie Wu, and Zhengyin Ye, from Northwestern Polytechnical University, China, published *Avoiding Choked Flow And Flow Hysteresis Of Busemann Biplane By Staggering Approach* in the Journal of Aircraft.[3] HUNS3D, an in-house Computational Fluid Dynamic (CFD) software, was utilized to generate the hybrid unstructured meshes and simulate supersonic flow over the biplane at various configurations. HUNS3D results were validated against Stanford's open-source CFD software, Stanford University Unstructured (SU2). The biplane simulated had a thickness to chord ratio of $t/c = 0.1$ with a constant horizontal gap of $0.5c$ between the leading edges. The mesh generated consisted of 122,512 elements. Spalart-Almaras turbulence model was used to simulate turbulence with a constant Reynolds number of 3.14106. An initial investigation on the effects of stagger were performed with the lower airfoil staggered longitudinally forward by increments of $0.25c$ up to $1.0c$. As this method showed promise in mitigating the choking phenomena, a continuous stagger method was set up to determine the optimal stagger distance while accelerating from $M=0.3$ to $M=2.5$.

The study concluded that the continuous stagger method experienced consistently lower drag through acceleration than the baseline Busemann biplane. More impressively, the continuous stagger method outperformed the diamond airfoil in the inviscid and viscous cases beyond $M=0.7$. It was determined that no stagger is beneficial beyond the design conditions. This method successfully reduced drag by nearly eliminating the flow choking and related hysteresis phenomena during off-design. [3]

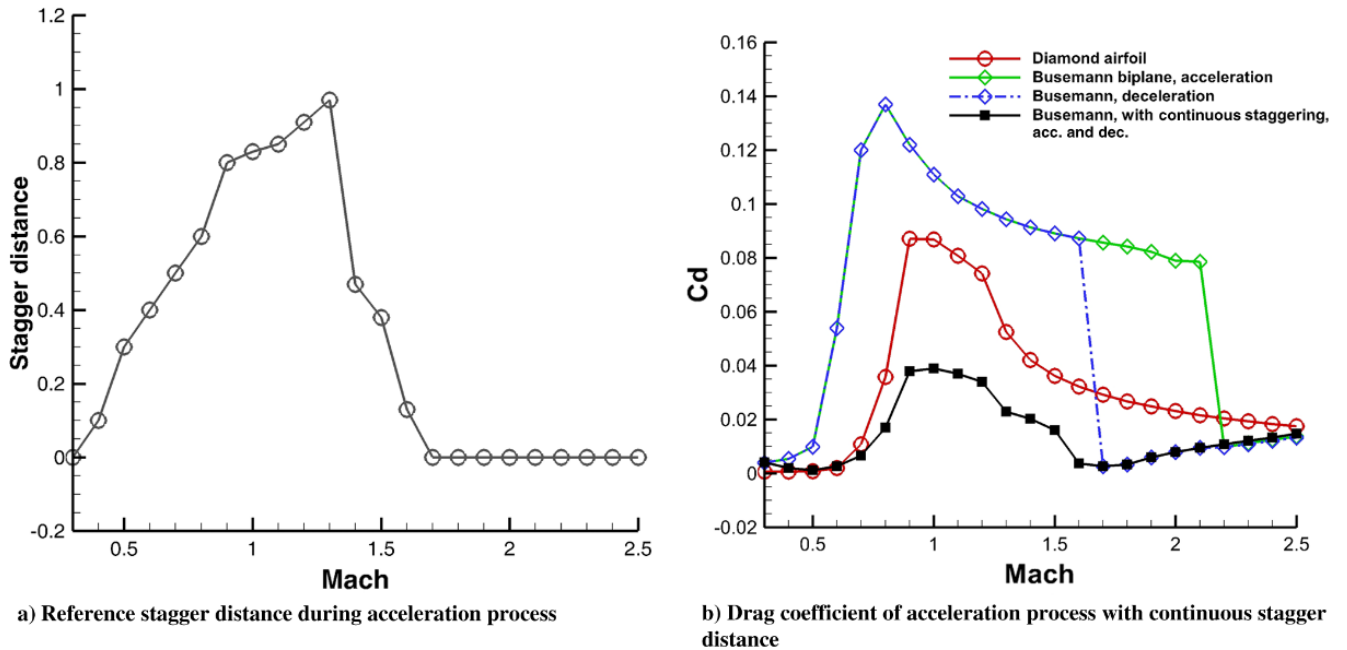


Figure 1. 4 - Drag coefficient of continuous staggered configuration in inviscid flow

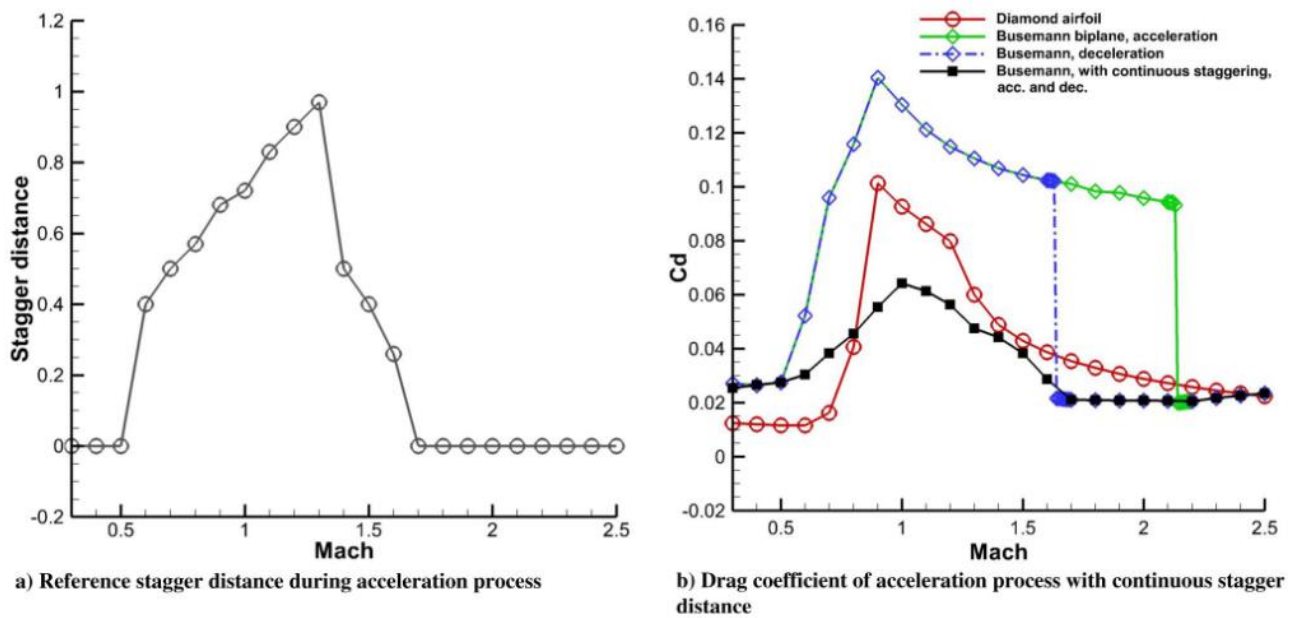


Figure 1. 5 - Drag coefficient of continuous staggered configuration in viscous flow

1.2.2 Major 2-D Modifications

1.2.2.1 High Lift Devices (HLD)

In 2008, Daigo Maruyama from the Department of Aerospace Engineering at Tohoku University in Sendai Japan, conducted a study entitled *Aerodynamic Design of Three-Dimensional Biplane Wings for Low Wave-Drag Supersonic Flight* which was published in the ICAS Archive.[4]

The study was multifaceted and addressed the topics of 2-D shape optimization, 3-D effects, finite 3-D wing optimization, and the utility of control surfaces to mitigate flow-choking. This section will discuss the results of investigation into the effectiveness of high lift devices to mitigate the flow-choking phenomena.

3-D CFD simulations were conducted using Tohoku University Aerodynamic Simulation (TAS) code with a three-dimensional unstructured grid to evaluate aerodynamic performance. The computations were conducted on the NEC SX-7 and NEC SX-9 supercomputers at the Cyberscience Center of Tohoku University. Design Mach number was 1.7, and total thickness-chord ratio was roughly at 0.1 after an optimization of the 2-D cross section. Following the optimization of the 3-D effects, a taper ratio of 0.25 was used for a wing platform reference area of 1. The ratio of horizontal gap to chord length was kept constant through the span of the 3-D wing. The slats and flaps were applied to this configuration with hinges at 0.3 c away from the leading and trailing edges respectively. Maruyama simulated this biplane configuration from take-off to cruise. Slat and flap positioning were changed throughout the flight duration. Results from this investigation, shown in figure 1.6 below, indicated that this method was effective at reducing the flow choking and hysteresis phenomena. Flow choking was eliminated at a freestream Mach number of 1.51. [4]

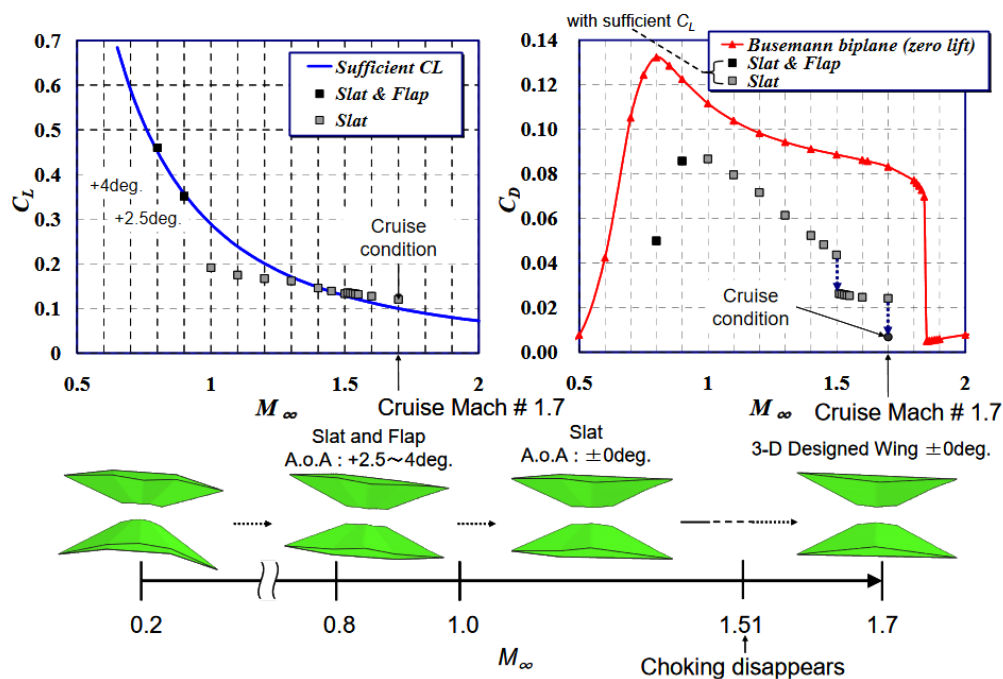


Figure 1. 6 - Lift and drag coefficients through simulated take-off to cruise conditions

These results are corroborated by the 2017 article *A Study of Busemann-type Biplane for Avoiding Choked Flow* published by the American Institute of Aeronautics and Astronautics.[5] Similar to Maruyama’s research, this team also focused on mitigating the flow choking and hysteresis phenomena through the implementation of slats and flaps. The team consisted of H. Yamashita and M. Yonezawa, graduate students at the Institute of Fluid Science at Tohoku University, S. Obayashi, Professor at the Institute of Fluid Science, and K. Kusunose, Senior Research Scientist at the Japan Defense Agency. Inviscid simulations were conducted using the Unified Platform for Aerospace Computational Simulation, UPACS, developed by JAXA. Simulations were run for three cases: Biplane with deflected leading edge flaps, biplane with deflected trailing edge flaps, and a biplane with deflected leading and trailing edge flaps. The baseline biplane design was developed in previous work by Kusunose and Obayashi. Results of this investigation are compared against the baseline biplane as well as a comparable diamond airfoil. Thickness to chord ratio of the biplane was set to $t/c = 0.05$. Slats and flaps are located $0.28c$ from the leading and trailing edge respectively. All flap deflections are such that the interior surfaces become parallel to the freestream.

For the deflected leading edge flaps scenario, the increase in drag related to the flow choking was successfully reduced relative to the baseline Busemann biplane. Flow choking was eliminated at a freestream Mach of 1.41 whereas the baseline continued to experience flow choking until Mach 1.63. The flow hysteresis range was also reduced relative to the baseline. The area ratio of this configuration was $A_t/A_i = 0.9$. These results are shown in figure 1.7 below. [5]

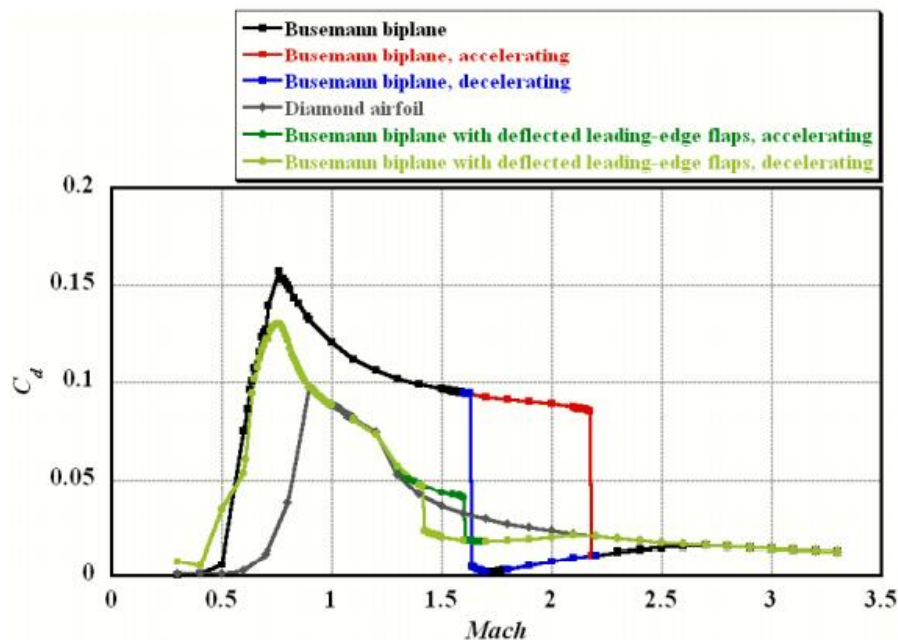


Figure 1. 7 - Drag coefficient comparison of leading edge deflected flap configuration compared against baselines

The deflected trailing edge flap scenario did not show beneficial results towards reducing drag or the flow hysteresis in supersonic flow. During supersonic conditions, the drag coefficient was consistently higher than the baseline biplane. However, this configuration did show a moderate reduction of drag in subsonic and transonic conditions. This scenario proved that trailing edge flaps are useful in reducing the wave drag in subsonic conditions. These results are shown in figure 1.8 below.

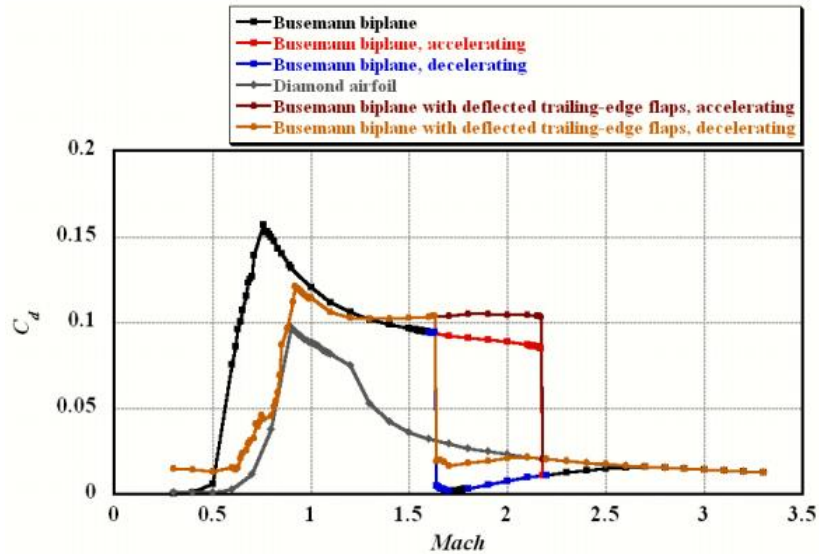


Figure 1. 8 - Drag coefficient comparison of trailing edge deflected flap configuration compared against baselines

In the final scenario, it was shown that the combination of leading edge and trailing edge flap deflections produced beneficial effects in both supersonic and subsonic flow conditions. Notably, this configuration displays a wave drag value close to that of the diamond airfoil at all Mach numbers. The region of flow hysteresis is reduced corresponding to the reduction in area ratio from the leading edge flap deflection while the transonic drag was reduced by the deflection of the trailing edge flaps. See figure 1.9 below. [5]

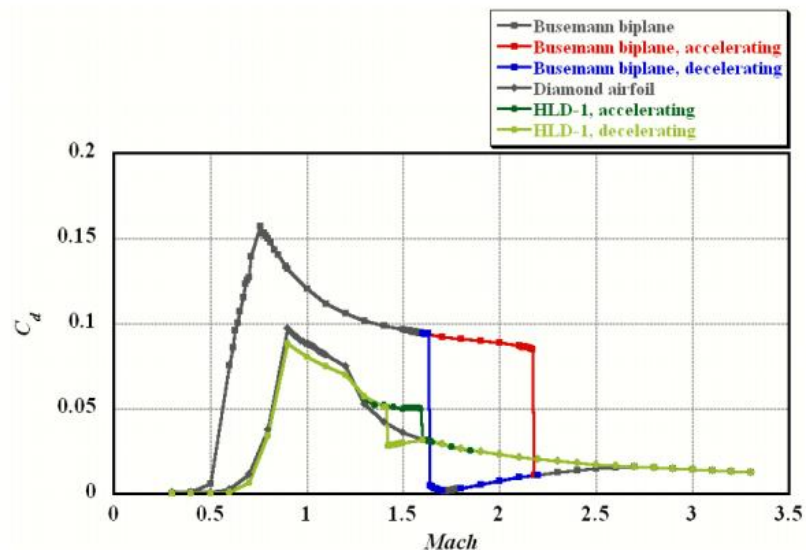


Figure 1. 9 - Drag coefficient comparison of configuration with both flaps deflected compared against baselines

1.2.2.2 Shape optimizations

In 2006, a paper was published in ICAS entitled *Numerical Design and Assessment of a Biplane as Future Supersonic Transport - Revisiting Busemann's Biplane*. [6] The study focused on three areas: applying an inverse problem approach to the biplane configuration to optimize the 2-D aerodynamic characteristics; analysis of performance at a variety of Mach speeds to determine variability; and a preliminary study for fuselage effects to eliminate sonic boom. For the inverse design method, the Licher model was used as a baseline at an angle of attack of $\alpha=1^\circ$. Licher type biplanes are identical to Busemann biplanes except that Licher type biplanes add the angle of attack to the lower body angles resulting in favorable wave interactions in lifting conditions. The total thickness to chord ratio was set to 0.1 with a vertical separation of $0.5c$ between the leading edges. Aerodynamic performance was conducted using TAS GRID and TAS Flow (in-house CFS software). TAS GRID was used to generate the unstructured mesh while TAS FLOW was used to solve for the Navier-Stokes/Euler flow. The design Mach number was set to 1.7.

To optimize the aerodynamic performance of the supersonic biplane, an inverse design method was implemented. The goals were as follows: to have the upper element generate more lift at the uppermost surface; to have the upper element generate more lift and thrust at the lower surface near the trailing edge; and to improve shock wave interaction at the throat. This was accomplished via a design loop wherein the pressure distribution around the designed biplane was compared against desired results. The difference between the desired results and simulated results were then used to modify the foil cross section. A detailed flowchart of this procedure is shown in figure 1.10 below.

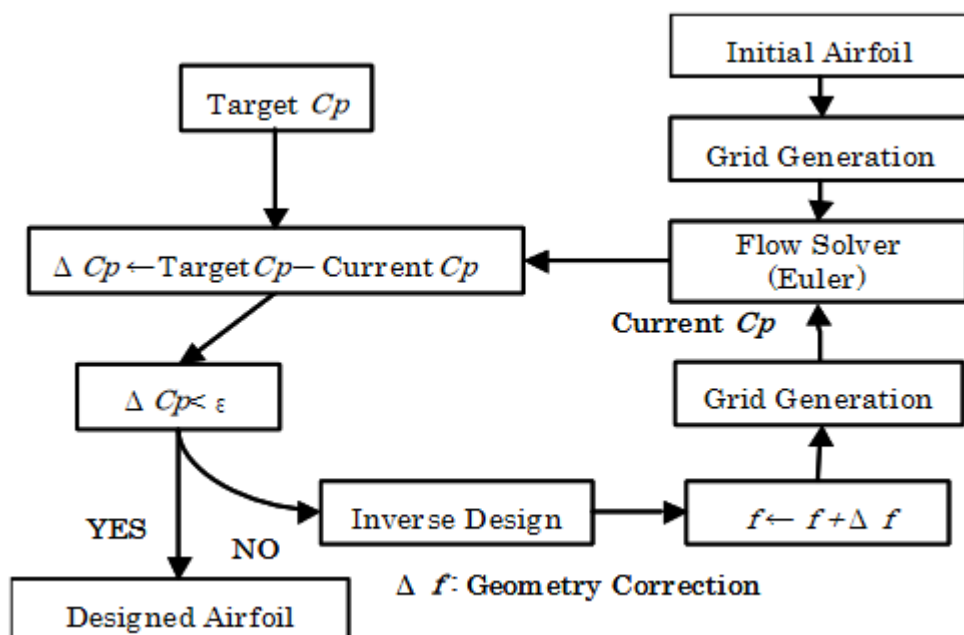


Figure 1. 10 - Flow chart showing inverse design methodology

The design converged after 14 iterations. The final design showed a reduction in thickness in the trailing edge of the upper airfoil. The lower surface of the upper airfoil developed a concave curvature, ultimately becoming parallel to the freestream at the trailing edge. Pressure peaks at the mid-chord throat were also greatly reduced. This was shown to improve the lift to drag ratio at the design conditions. The designed biplane had a Lift to drag ratio of $L/D=22$ whereas the baseline biplane had a lift to drag ratio of $L/D=18$. A comparison between the designed biplane and baseline as well as the pressure contours are shown in figures 1.11 and 1.12 below. [6]

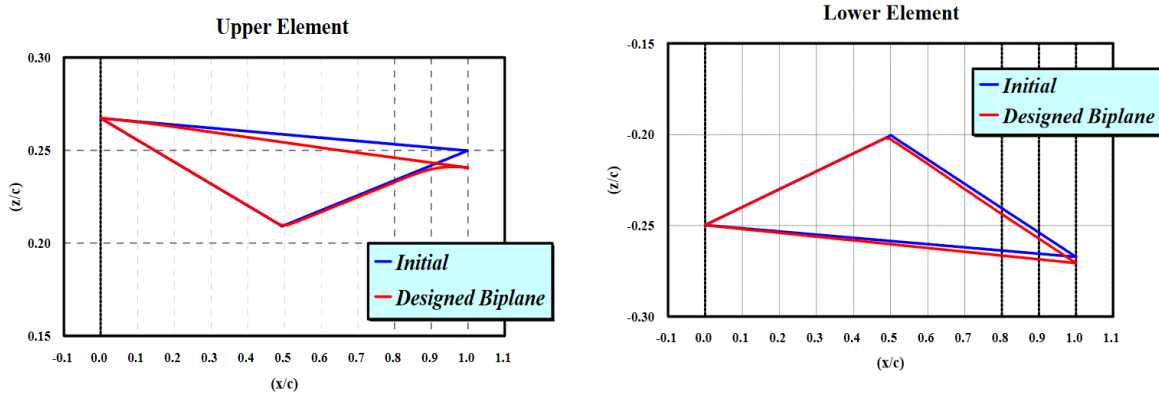


Figure 1.11 - Cross-sectional diagram of the design biplane surfaces

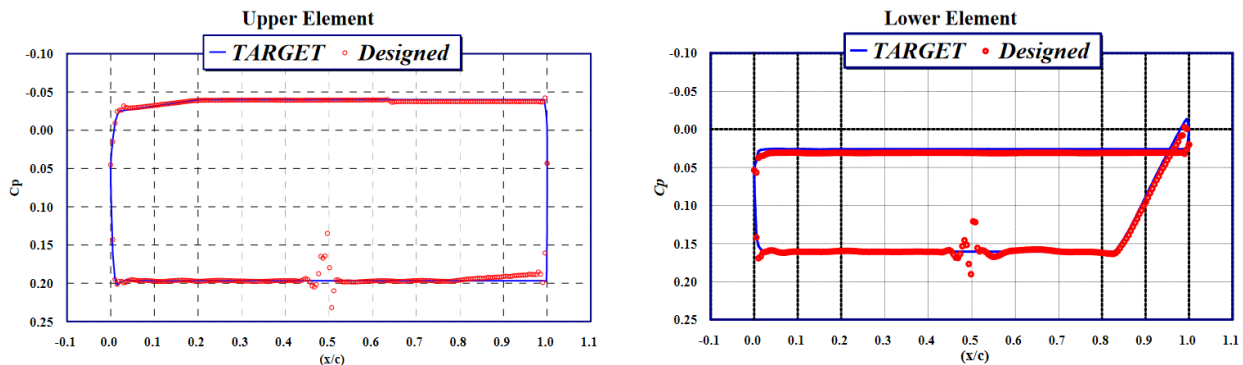


Figure 1.12 - Pressure coefficient of the designed biplane compared against the intended results

In 2020, an article entitled *Design of a New Supersonic Biplane* was published in Elsevier. Contributing authors were Jian Zhai and Wei-Wei Zhang from the National Key Laboratory of Aerodynamic Design and Research, Northwestern Polytechnical University, Xi'an Shaanxi, and Chen-An Zhang and Fa-Min Wang from the Institute of Mechanics, Chinese Academy of Sciences, Beijing. [7] The goal of this study was to develop a new supersonic biplane with beneficial wave cancelation effects similar to the Busemann biplane while reducing the flow choking phenomena during off-design conditions. Referencing the work of Patadir et al. [2], the flat plate was staggered laterally backwards relative to the triangular airfoil. The optimum position of the flat plate was calculated by oblique shock theory and Prandtl-Meyer theory. The flat plate was approximated by a rectangle with a width of $0.001c$ and rounded ends of diameter $0.001c$. The new supersonic biplane was designed for Mach 2. This is shown in the figure below.

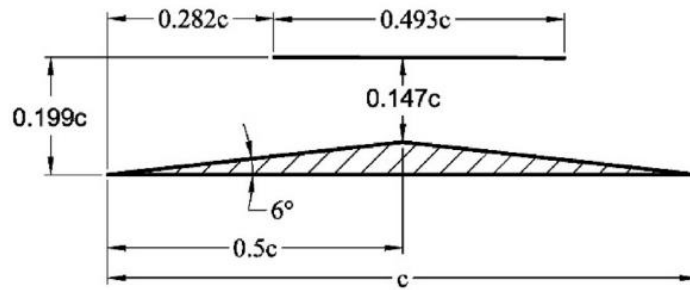


Figure 1.13 - Cross section of proposed new supersonic biplane

CFD calculations were conducted using Reynolds-averaged Navier-Stokes equations as well as Euler equations. The turbulent model used was the Shear-Stress transport (SST). Sutherland's Law was used to calculate the viscosity coefficient and thermal conductivity. The gas was assumed to be calorically perfect. A mesh independence study was performed at a Mach number of 2 at zero angle of attack. The four grids consisted of approximately 0.1, 0.2, 0.4, and 0.8 million nodes. It was determined that mesh independence was achieved at approximately 0.4 million nodes.

Results of the study showed that this design successfully reduced drag as well as the related flow hysteresis relative to the baseline Busemann biplane. At design conditions, a 12.7% increase in lift to drag ratio was observed. At off design conditions, wave drag reduction was noted through all Mach numbers relative to the baseline. This implied that potential benefits may be achieved by replacing one or both compressive wedges with shock-reflecting flat surfaces.[7]

In 2016, IntechOpen published an article entitled *Shape Optimization of Busemann-Type Biplane Airfoil for Drag Reduction Under Non-Lifting and Lifting Conditions Using Genetic Algorithms*, by Yi Tian and Ramesh Agarwal, from the Department of Mechanical Engineering and Materials Science at Washington University in St. Louis, Missouri.[8] Similar to the other articles reviewed, the goal of the study was to investigate methods for optimizing the shape of the Busemann-type biplane airfoil to reduce drag for non-lifting and lifting conditions. The difference in their approach, however, was that genetic algorithms were employed.

A baseline Busemann biplane with a design point at Mach 1.7 was selected, corresponding to a thickness to chord ratio, t/c of 0.05 for both the upper and lower airfoils. The CFD software used was ANSYS Fluent. Flow was assumed to be inviscid. ANSYS ICEM software was used to generate the structured H-grid mesh around the airfoils. A rectangular far-field was employed. A standard grid was created for the baseline Busemann biplane, which was then applied to the generated designs using ICEM. Three flow conditions were simulated: a uniform impulsive flow, an accelerating flow, and a decelerating flow.

To generate optimized Busemann biplane airfoils for lifting and non-lifting conditions, two types of genetic algorithms were employed. A single-objective genetic algorithm (SOGA) was used to minimize drag under non-lifting conditions and a multi-objective genetic algorithm (MOGA) was used to maximize both lift and lift to drag ratios under lifting conditions. The genetic algorithm employed six steps: Initialization - random generation of a population of

airfoils; Evaluation - determination of the fitness of each airfoil; Natural selection - removal of the lowest performing airfoils; Reproduction - pairing of airfoil combinations to create offspring; Mutation - random modification of a small percentage of the population; and finally, a check for convergence. In the initialization phase, a population of random foils are generated by applying a random Bezier curve to the inner surfaces while the curvature of the outer surfaces was modified to maintain identical thickness to the baseline biplane. In the zero-lift condition case, the airfoil was then mirrored to create the biplane cross sectional profile to generate a symmetrical airfoil. In the case of lifting conditions, separate Bezier curves were generated for all internal surfaces, thus generating an asymmetric biplane configuration. MATLAB was used to generate the Bezier curves.

The fitness function implemented within the SOGA was an average of the drag coefficients across Mach numbers from 1.1 to 1.7. After 20 generations with a population of eight, the SOGA converged. The optimized design is shown in figure 1.14 below:

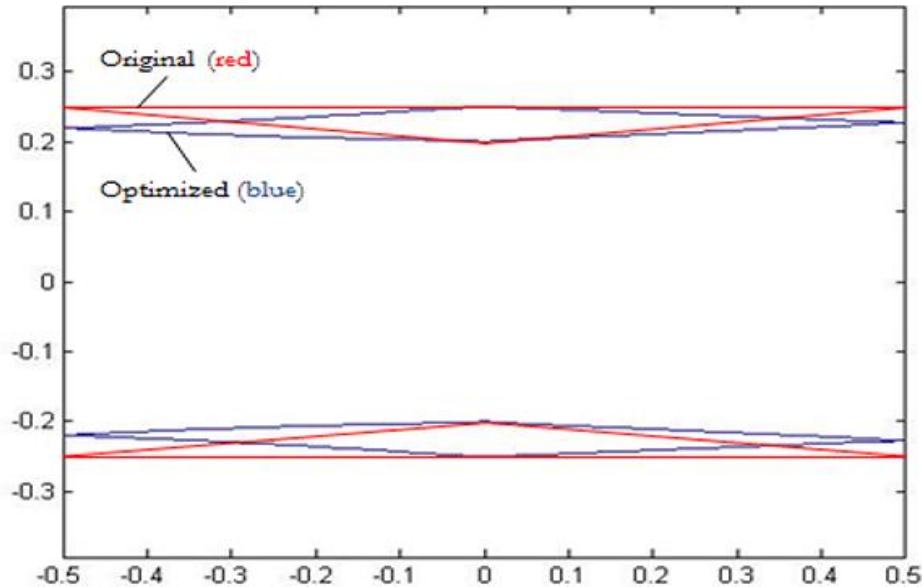


Figure 1. 14 - Cross-section of the generated symmetrical biplane airfoil compared (blue) against the baseline (red)

Their findings indicate that the optimized symmetric airfoil hysteresis range is reduced to Mach 1.3 to Mach 1.5. For both acceleration and deceleration, choked and unchoked, the optimized design generated less drag than the baseline. However, it can also be seen that the baseline experienced less drag at the design condition of Mach 1.7 during deceleration. See figure 1.15 below.

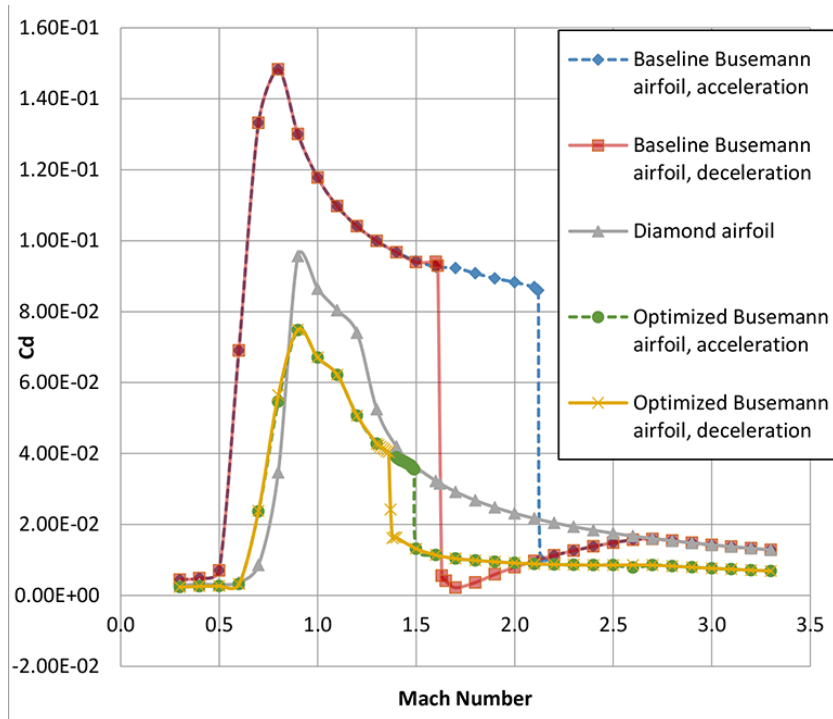


Figure 1. 15 - Comparison of drag coefficient across flight Mach numbers for symmetric generated biplane against baselines

Similar to the SOGA, the fitness functions implemented within the MOGA were averages of the lift and drag coefficients across the seven design points between Mach 1.1 and 1.7. The objective was to maximize lift while minimizing drag. After 20 generations with a population of eight, the MOGA converged. The optimized design is shown in figure 1.16 below.

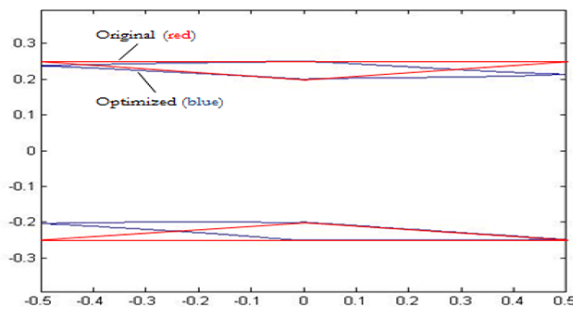


Figure 1. 16 - Cross-sectional comparison of the generated asymmetrical biplane (blue) against the baseline (red)

Their findings indicate that the optimized asymmetric airfoil hysteresis range is reduced to Mach 1.6 to Mach 1.3. For both acceleration and deceleration, choked and unchoked, the optimized design generated less drag than the baseline. However, it can also be seen that the baseline experienced less drag at the design condition of Mach 1.7 during deceleration. See figure 1.17 below. [8]

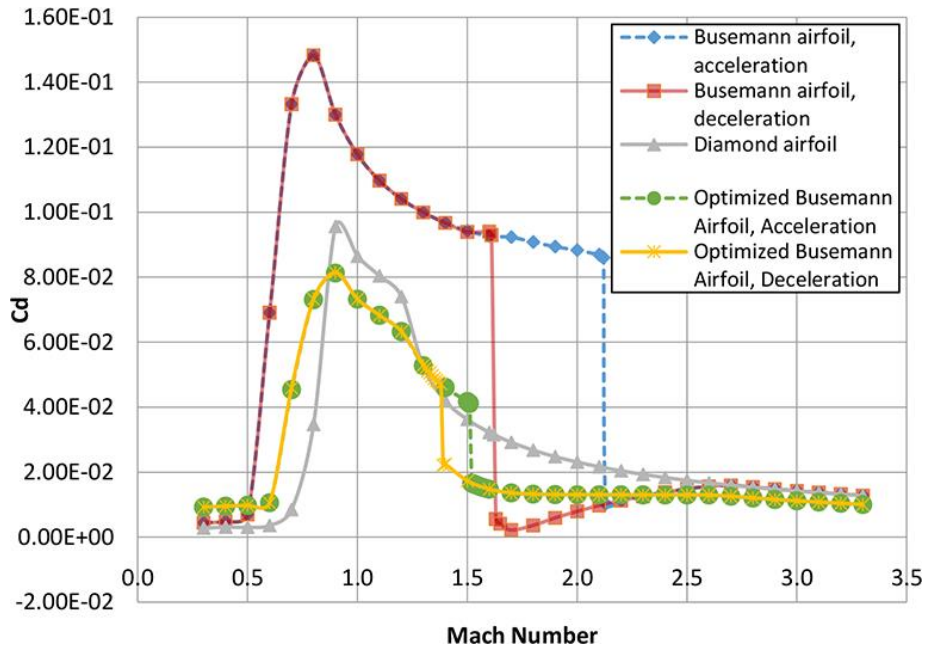


Figure 1. 17 - Comparison of drag coefficient across flight Mach numbers for asymmetric generated biplane against baselines

1.2.3 3-D Considerations

In 2011, Elsevier published an article called *Supersonic Biplane - a Review*, written by Kazuhiro Kusunose from JAXA, Japan, Kisa Matsushima from the University of Toyama, Japan, and Daigo Maruyama from ONERA, France.[9] All three authors have been cited for their studies and results earlier in this paper. The 2011 article built upon the results of these earlier efforts and was multifaceted covering the topics of 2-D shape optimization, 3-D effects, finite 3-D wing optimization, and the utility of control surfaces to mitigate flow-choking. This portion of the literature review focuses on the 3-D effects and finite 3-D wing optimization.

A rectangular wing was created by extruding out the 2-D cross-section. The wing reference area, semi-span length and aspect ratio were chosen to be $1.0 m^2$, 1.0 m, and 2.0 respectively. Not surprisingly, the CFD calculations showed poor results compared to the 2-D model due to interference from the Mach cones generated by the wing-tips. To mitigate the wing-tip effects, a taper ratio of 0.25 was added to the wings, corresponding to an aspect ratio of 5.12. This necessitated a dihedral angle on the lower platform and an anhedral angle on the upper platform. New CFD calculations confirmed the benefits of this modification as shown on the figure 1.18 below.

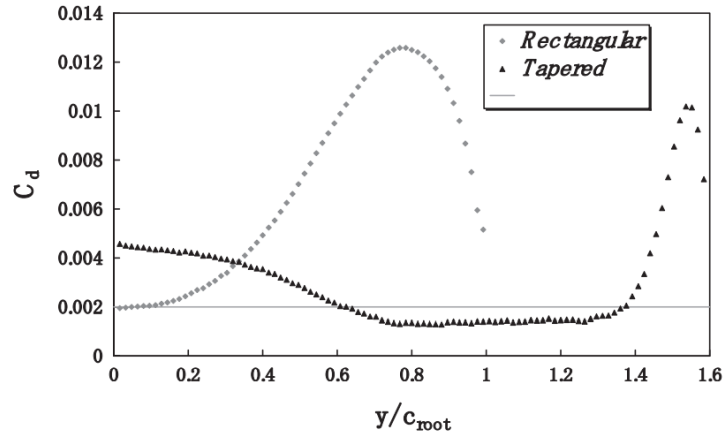


Figure 1.18 - Drag coefficient comparison of rectangular wing platform and tapered wing platform

Following this, an investigation into the effects of sweep angle was conducted. Sweep angle is defined as the angle between the leading edge and the freestream. Case 1 has no sweep, and Case 2 is swept such that the mid-chord is perpendicular to the freestream. A lower C_d is observed for Case 2 as compared to Case 1. This is shown in figure 1.19 below.

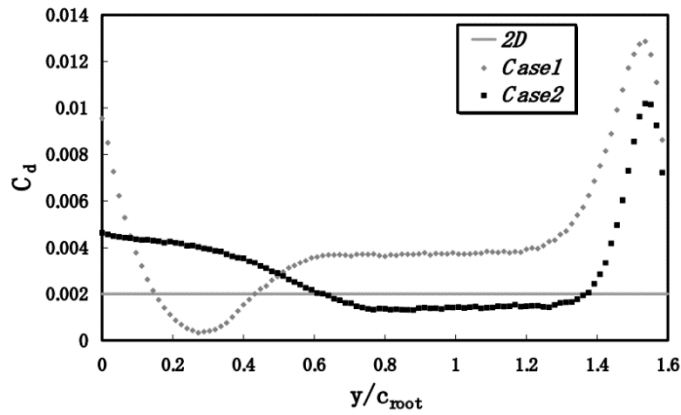


Figure 1.19 - Drag coefficient comparison of sweep cases

To deal with the Mach cone effect, winglets were added which close the ends of the wings, thereby constraining the shockwaves internally. A significant reduction in drag as well as shock cone effects was observed with the box wing configuration; C_d without winglet was 0.00300 while the C_d with the winglet was 0.00258. See figure 1.20 below.

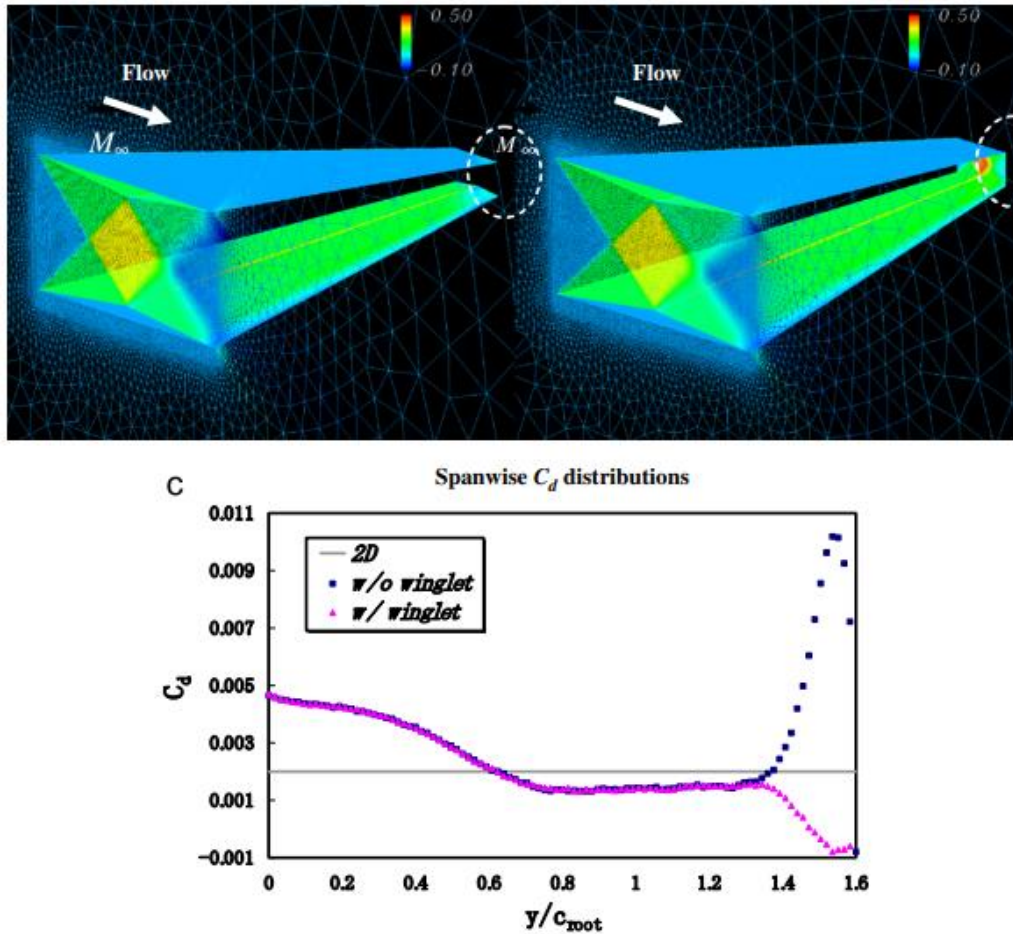


Figure 1.20 - Drag comparison of box winglet vs open biplane configurations

Lastly, an aerodynamic taper was applied via the inverse design method every $0.1c$ along the wingspan. The inverse design method was described in *Numerical Design and Assessment of a Biplane as Future Supersonic Transport - Revisiting Busemann's Biplane* and discussed above. The optimization process was performed along the upper surface while maintaining the lower surface as cross-sectionally consistent. Following this, the lower surface was optimized along the wingspan while maintaining the new upper surface as cross-sectionally consistent. CFD was performed after each step and compared against the original configuration. This was shown to have moderate improvement to both lift and drag, especially near the root as demonstrated in the figures below. [9]

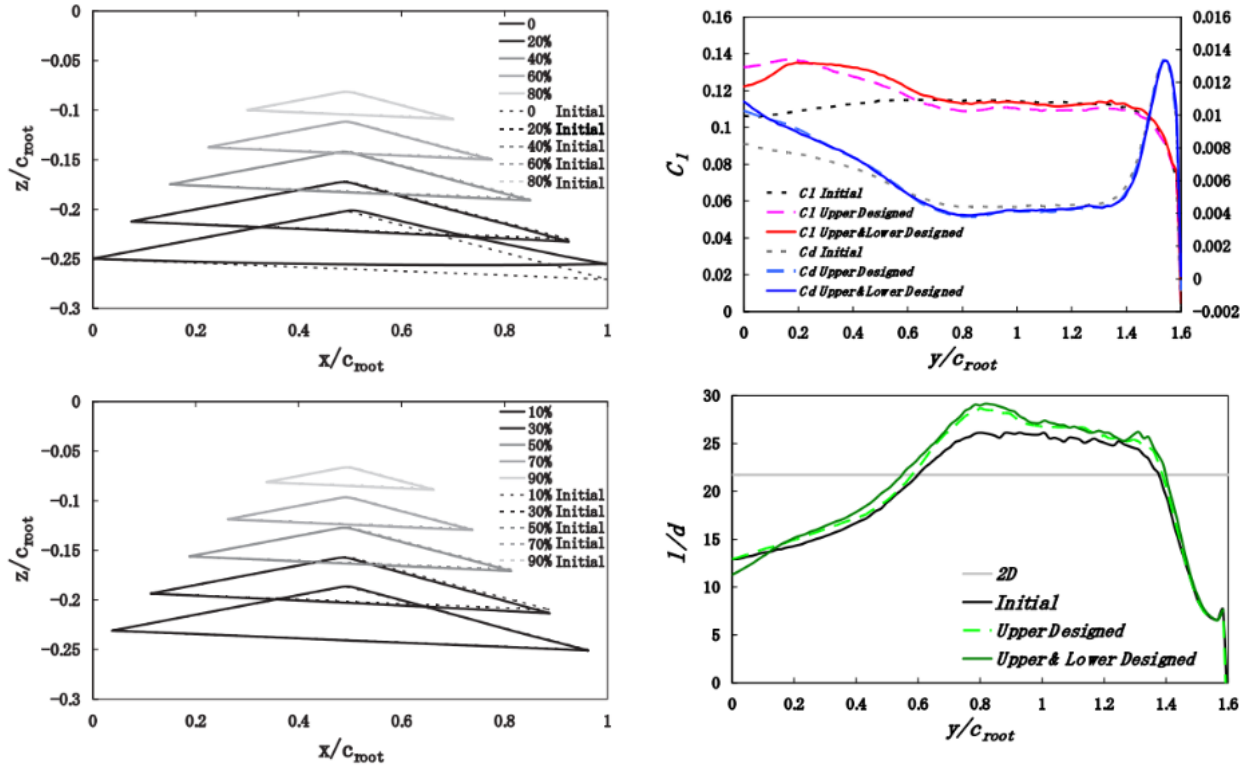


Figure 1. 21 - Cross sectional depiction of applied aerodynamic taper. Lift to drag ratio and lift coefficient along the wingspan of the results of the inverse design method

1.2.4 Historical Data Comparison

Several methods have been proposed to address both the hysteresis phenomena as well as the flow choking problem. Some of these methods have been reviewed in the literature review contained in chapter 1 of this paper. These methods include: altering the cross-sectional profile of both of the airfoils; changing the relative position of the two airfoils, both statically and dynamically; and utilizing actuating flaps on the leading and trailing edges of both of the biplane surfaces. What follows is a comparison between some of the reviewed design modifications. Each biplane compared started from a baseline biplane designed for Mach 1.7 flight – the thickness to chord ratio of both baseline foils was $t/c = 0.05$ with wedge angles of 5.7 degrees.

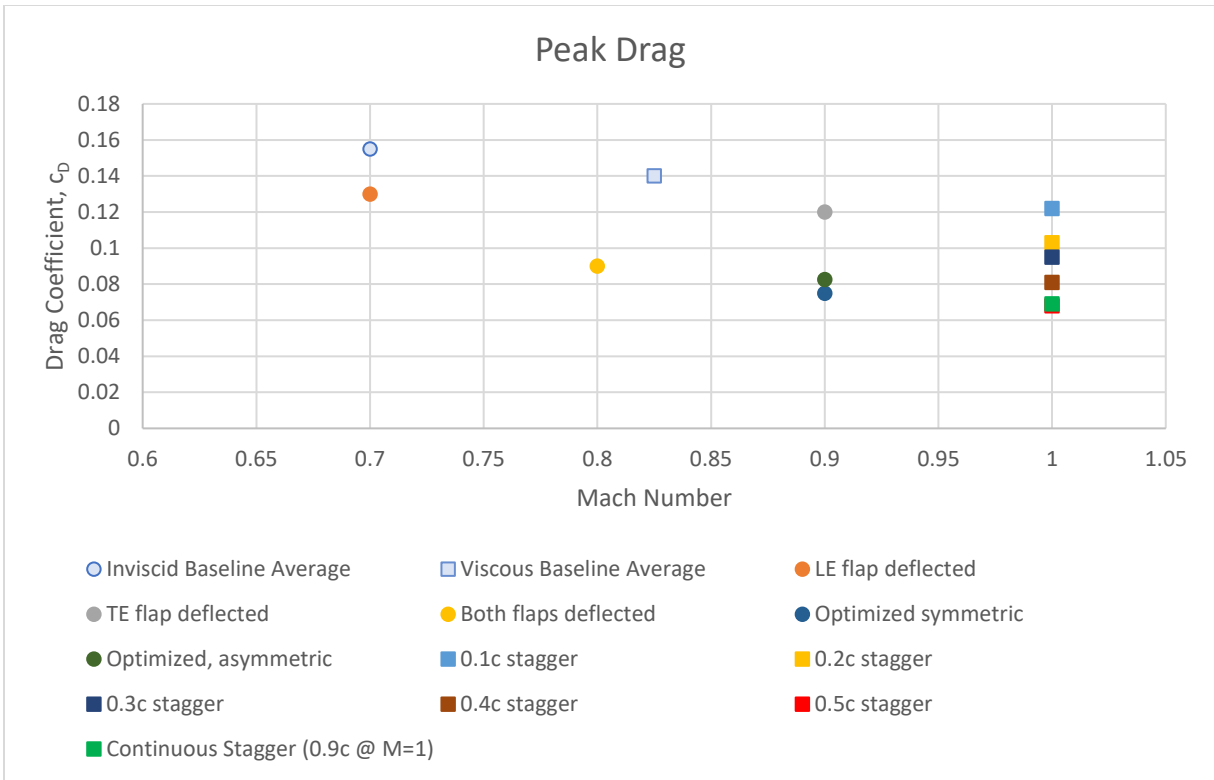


Figure 1. 22 – Comparison of the inviscid vs viscous laminar drag coefficients of historical data

The above graph shows the peak drag generated by the reviewed design modifications in comparison with the baseline. Peak drag is a good means of determining the amount of flow choking that occurs from one design to another. Due to limitations on available data, inviscid results are included here with viscous results. Inviscid results are displayed with dots, while viscous results are displayed with squares. The above results show that staggering, even when including viscous effects, reduce the peak drag to a greater degree. Interestingly, the methods of stagger between the two studies considered are opposite, with one staggering the top foil forward while the other staggers the top foil backwards, yet the results are nearly identical for peak drag. This shows that airfoil stagger is an effective way to mitigate the amount of choking a Busemann biplane will experience.

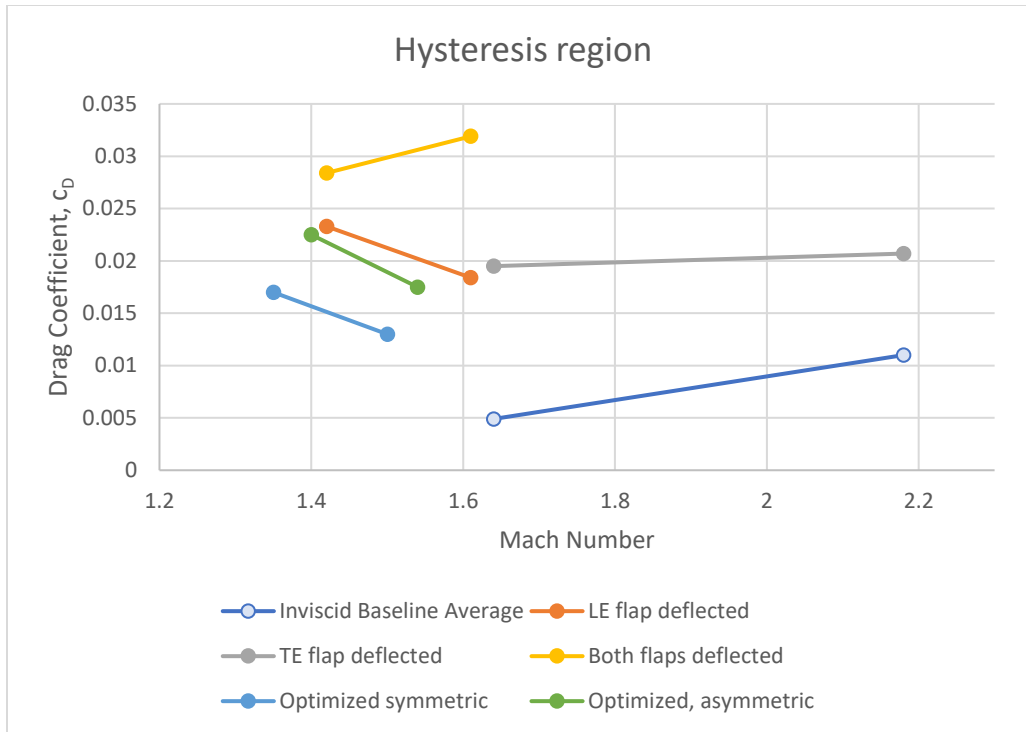


Figure 1. 23 – Comparison of hysteresis regions compared to baseline

The above graph shows a comparison of the hysteresis regions for the reviewed design modifications in comparison with the baseline. Unfortunately, only the inviscid results are shown here as hysteresis was not investigated in the papers pertaining to stagger. The above graph shows that curvature modifications to the leading edges of the airfoils has a great effect on reducing the hysteresis region, while changing the curvature on the trailing surfaces has little to no beneficial effect regarding hysteresis reduction. Modifying the full length of the leading edge surfaces was shown to be more effective than simply implementing the use of leading edge flaps for this purpose. The Bezier curve biplanes had considerably smaller hysteresis regions with generally lower drag than the flapped Busemann biplane. The asymmetric Bezier design had a slightly smaller hysteresis region than the symmetric Bezier biplane design. The asymmetric design spanned for a Mach range of 0.14 while the symmetric design hysteresis region spanned for 0.15.

1.3 Project Proposal

This project seeks to further optimize the Busemann biplane airfoil design. Much of the research conducted has been relatively limited in scope, performing minor surface curvature optimization, altering the relative position of the two airfoils, or implementing control surfaces. There is the potential to further optimize the concept of a supersonic biplane by varying numerous design parameters at once. This project will investigate the impacts of employing design optimization across multiple design variables. The focus will be to reduce wave drag by mitigating flow choking at off-design conditions, thereby positively affecting the aerodynamic coefficients. Additional considerations will be taken to address the hysteresis phenomena.

The optimization schemes will employ a larger design space than have been utilized in recent years. Additional design considerations include relative position, wedge angles and chord lengths. Relative position references the position of the foils in space relative to one another. All of these design considerations will be included in the analysis.

Chapter 2 – Background

2.1 Overview of Supersonics

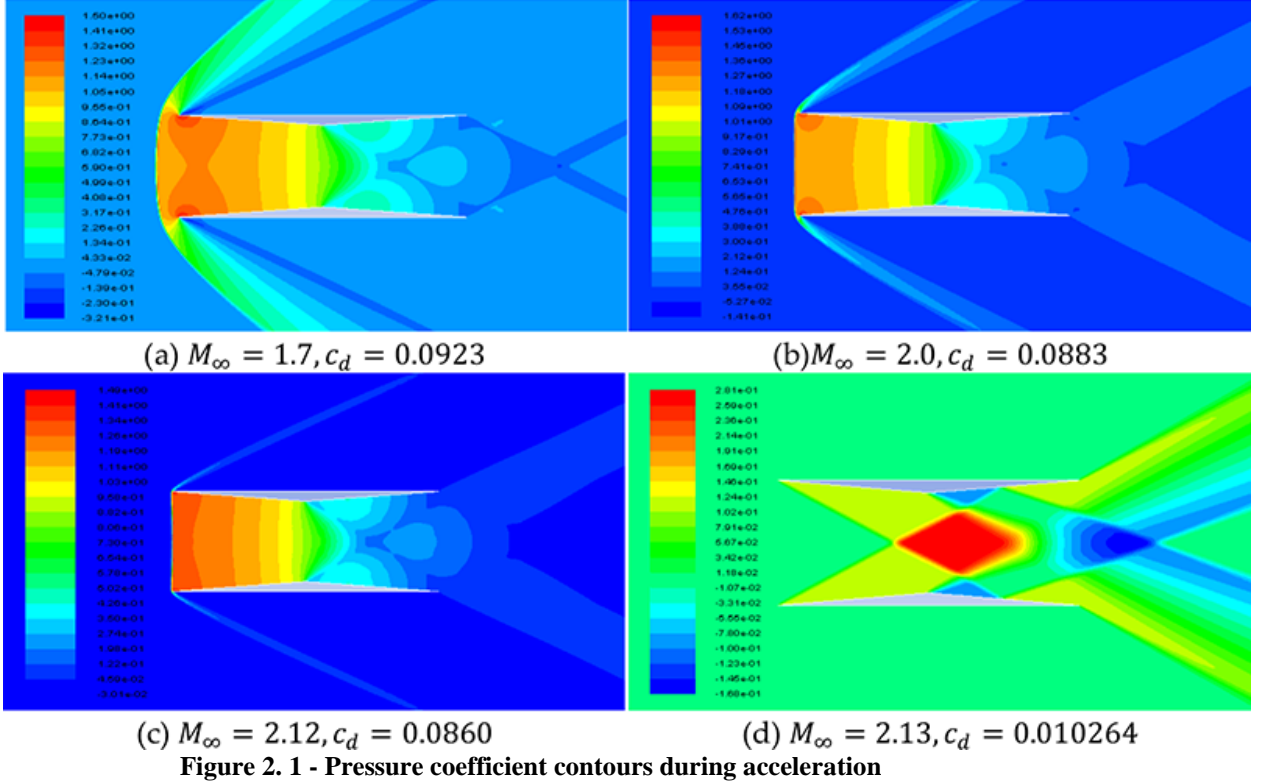
The following is the necessary background to understand the Busemann biplane and the analysis methods employed.

2.1.1 Bow Shocks Shock Waves

The Busemann biplane is designed to operate at supersonic speeds. Any object traveling through a fluid at supersonic speeds generates shock waves, across which properties of the flow change discontinuously and entropically – pressure and temperature are increased while flow velocity is drastically decreased. In the low Mach regime, detached shockwaves form a short distance upstream.

During acceleration, the Busemann biplane and other double triangular wedge airfoil designs experience some amount of detached shock formation. These detached shocks, or bow shocks, have dramatic effect on the flow, reducing the velocity to super-sonic conditions almost instantaneously. The flow between the biplane surfaces is essentially choked at the inlet as the bow shock generated at transonic speeds stretches between the two leading edges. The formation of this bow shock causes the dramatic increase in drag seen in the prior drag coefficient vs Mach number plots. The reasons for this increase in drag are well explained in Anderson's Fundamentals of Aerodynamics Chapters 7, 8, 9, and 11 [10]. As the flow is reduced to below sonic conditions and can therefore no longer be treated as inviscid, formulation of this region is complex. No beneficial shock-shock interactions may be found in this region.

References 2, 3 and 5 as well as figure 2.1 show that the amount of drag generated is directly related to the cross-sectional area. These bow shocks often persist beyond the transonic flow regime. These papers describe how the bow shock persists until the shockwave is compressed close enough to the airfoil's leading edges to be swallowed in between the two surfaces.



2.1.2 Shock Expansion Theory

Once the bow shock is sucked in between the two airfoil surfaces, the shockwaves adhere to the surfaces and project at oblique angles. Attached shocks may be described by the rules and formulas of established shockwave theory. Flow downstream of an oblique shock will always be parallel to the surface that necessitated the change in flow angle. The angle at which the shockwave will form may be calculated through the θ - β - M relation which relates upstream Mach number, M_1 , turn angle, θ , and shock angle, β .

$$\tan \theta = 2 \cot \beta \left[\frac{M_1^2 \sin^2 \beta - 1}{M_1^2 (\gamma + \cos 2\beta) + 2} \right] \quad (2.1)$$

Following this, the perpendicular component of the local Mach number may be used to calculate the downstream flow properties of an oblique shock via the normal shock relations. That is:

$$M_{n,1} = M_1 \sin \beta \quad (2.2)$$

$$\frac{P_2}{P_1} = 1 + \frac{2\gamma}{\gamma+1} (M_{n,1}^2 - 1) \quad (2.3)$$

$$\frac{\rho_2}{\rho_1} = \frac{(\gamma+1)M_{n,1}^2}{2+(\gamma-1)M_{n,1}^2} \quad (2.4)$$

$$\frac{T_2}{T_1} = \frac{P_2 \rho_1}{P_1 \rho_2} \quad (2.5)$$

$$M_{n,2} = \sqrt{\frac{1 + \left[\frac{\gamma-1}{2}\right] M_{n,1}^2}{\gamma M_{n,1}^2 - \frac{\gamma-1}{2}}} \quad (2.6)$$

As this change in flow direction is compressive, it makes sense that downstream pressure, density, and temperature would increase in proportion to the perpendicular component of the flow Mach number. As a result, flow properties change less dramatically downstream of oblique shocks than detached shocks. Unlike detached shocks, flow moving downstream of an attached shock is not necessarily subsonic. Downstream Mach number may be found through trigonometry.

$$M_2 = \frac{M_{n,2}}{\sin(\beta-\theta)} \quad (2.7)$$

Expansion waves, sometimes called expansion fans, form as a consequence of supersonic flow turning out of itself – e.g., when the area available to the fluid particles is increased as flow direction changes [10]. Unlike shockwaves, expansion waves are wide regions across which flow properties change. Through an expansion wave the local temperature, pressure, and density are seen to decrease as flow velocity increases. These changes occur with little to no increase in local entropy; thus, the isentropic relations apply. The method to calculate the flow properties downstream of an expansion wave is Prandtl-Meyer Expansion Theory, which hinges on the relationship between turn angle, θ , and the upstream and downstream values of the Prandtl-Meyer function, $\nu(M)$.

$$\nu(M) = \sqrt{\frac{\gamma+1}{\gamma-1}} \tan^{-1} \left(\sqrt{\frac{\gamma-1}{\gamma+1} (M^2 - 1)} \right) - \tan^{-1} \sqrt{M^2 - 1} \quad (2.8)$$

$$\theta = \nu(M_1) - \nu(M_2) \quad (2.9)$$

The downstream Mach Number, M_2 , can be found through algebraic manipulation of the above formulae. The corresponding downstream flow properties may be found through the application of the isentropic relations:

$$\frac{T_2}{T_1} = \frac{1 + \left(\frac{\gamma-1}{2}\right) M_1^2}{1 + \left(\frac{\gamma-1}{2}\right) M_2^2} \quad (2.10)$$

$$\frac{P_2}{P_1} = \left(\frac{\rho_2}{\rho_1}\right)^\gamma = \left(\frac{T_2}{T_1}\right)^{\frac{\gamma}{\gamma-1}} \quad (2.81)$$

These formulae, used in conjunction, are the basis of shock-expansion theory.

In addition to the above, it is important to understand that there are cases when shockwaves will interact with surfaces or other shockwaves. The case of shockwave reflection is simple enough, as a new wave forms at the point of impingement in response to the flow angle changing to match that of the surface. Shock-shock interactions are more complicated. In this case, both shockwaves are refracted to a certain degree, corresponding to flow conditions. To

solve for this, it is important to understand that the pressure downstream of refracted shockwaves must be equal and the flow angle must be the same [10]. Taking this into consideration, it is possible to iterate through possible combinations of refracted shockwave angles until a correct solution is found.

2.1.3 The Method of Characteristics

An alternative means of calculating flow properties through a flow field is the Method of Characteristics. Like shock-expansion theory, the method of characteristics is a purely theoretical method which assumes flow is inviscid, steady, supersonic, two-dimensional, and irrotational [10]. This method forms a grid of characteristic lines along which the derivatives of flow field values are indeterminate. These indeterminate derivatives serve as guidelines for areas of flow domains wherein the partial differential governing equations simplify to algebraic relations.

Characteristic lines are classified into families in the same manner as shockwaves; lines of positive slope are considered “left running” and referred to as C_+ while those with negative slope are considered “right running” and referred to as C_- . The angle of a characteristic line is the Mach angle at that point, that is:

$$\mu = \sin^{-1} \frac{1}{M} \quad (2.92)$$

Characteristic lines maintain a constant value through their length, relating flow values; K_+ and K_- for the left and right running characteristic lines respectively. The flow values of θ and M may be calculated at any point of intersection p on the characteristic mesh if the values of K_+ and K_- are known for the given intersection. The formulation of these flow values is exact; however, approximation must be taken in determining the location. In reality, characteristic lines are curved. For the purposes of calculation, this curvature is neglected, and characteristics are approximated as straight line segments.

Table 2.1 – Characteristics definition

Symbol	Family	Approximate slope formula	Constant
C_+	Left Running	$(+) \frac{\theta_+ + \theta_p + \mu_+ + \mu_p}{2}$	$\theta - \nu(M) = const = K_+$
C_-	Right Running	$(-) \frac{(\theta_+ + \theta_p) - (\mu_+ + \mu_p)}{2}$	$\theta + \nu(M) = const = K_-$

2.1.4 Aerodynamic Forces

The two primary aerodynamic forces are lift and drag. Lift is generally considered as upward force in opposition to gravity while drag is any force acting in opposition to travel through a given fluid. Moving forward, it will be important to understand the pressure-based definition of lift and drag.

2.1.4.1 Lift

There are multiple competing definitions of lift that seek to quantitatively define the upward force generated by flow over a surface. One method is the pressure-based definition of lift. This states that lift force is generated by the difference in pressure between the surfaces of a given object. It makes sense that if the lower surface of an airfoil experiences higher pressures than the upper surface, then there will be a net upwards force on the foil. This definition functions well in supersonic flow where pressures tend to be constant along surfaces. Figure 2.2 below is an example of the graphical calculation of pressure drag around a flat plate at an angle of attack in supersonic flow.

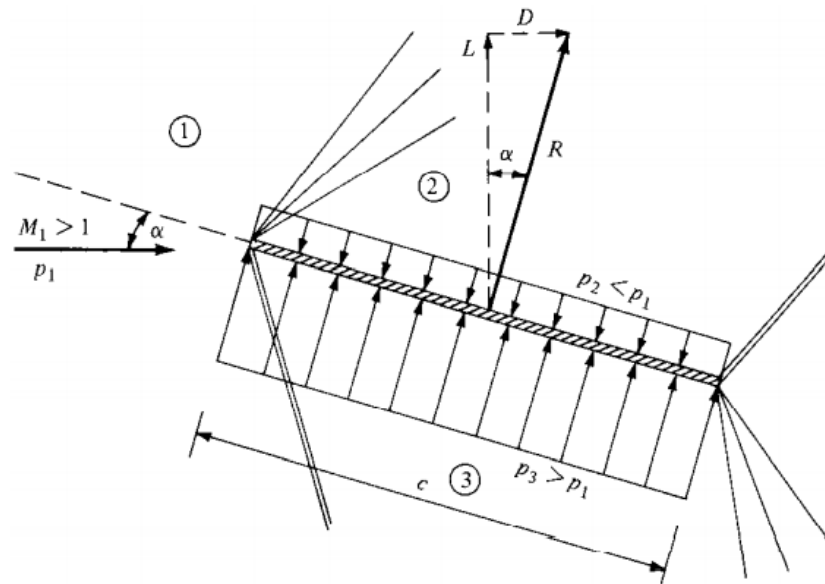


Figure 2. 2 - Flat plate at an angle of attack [10]

2.1.4.2 Drag

Qualitatively, drag is defined as any force generated by a fluid that works in opposition to an object's motion through the fluid. Quantitatively, drag can be difficult to define due to the numerous factors that contribute to the total drag. In the subsonic regime, frictional effects tend to dominate the drag calculation. At supersonic speeds, however, the overall shape of an object or craft is the primary source of drag.

2.1.4.3 Friction Drag

Viscosity is an inherent property of a fluid that can be likened to friction within the fluid and is a measure of a fluid's resistance to changes in velocity. As an object travels through a given fluid, it will push against the fluid, altering the local velocity of fluid particles near the object. This creates a boundary layer wherein the flow transitions from the speed of the object to the speed of the freestream. The fluid, in turn, resists this change in velocity, pushing back against the object with a force proportional to the viscosity of the fluid. This phenomenon gives rise to an element of drag referred to as friction drag.

Friction drag predominately occurs when an object is traveling at lower speeds. Functionally, this is due to the amount of time individual particles of a fluid are affected by the object in motion. As an object travels faster, the fluid particles have less time to interact, thus reducing the friction drag exerted on the object.

2.1.4.4 Wave Drag

At high enough speeds, the effects of viscosity are negligible, and the flow can be reasonably assumed to be inviscid, e.g., without viscosity. While this assumption does result in zero friction drag, there is still non-zero total drag due to pressure differences. At supersonic speeds where shockwaves develop, an additional form of drag arises as consequence of the non-isentropic nature of shockwaves. This is referred to as wave drag and may be calculated through the differences in the longitudinal components of the pressure experienced by an object traveling at supersonic speeds. The mitigation of wave drag is of considerable importance in designing an aircraft or wing for supersonic flight.

2.2 Overview of the Busemann Biplane

2.2.1 Design logic

The Busemann biplane was first proposed by Adolf Busemann in the 1935 paper, *Aerodynamischer Auftrieb bei Überschallgeschwindigkeit*. The design consisted of two opposing triangular surfaces mirrored across a central axis with the peaks forming a throat in the center. In essence, it is a diamond airfoil that has been divided along the center line, then inverted. This configuration is often likened to a de-Laval nozzle without a tank. [9]

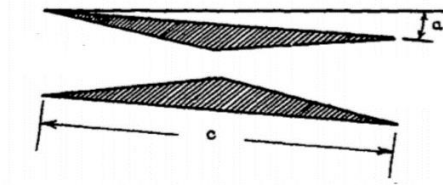


Figure 2. 3 - Busemann biplane at angle of attack [1]

The design Mach of a Busemann biplane is defined by the wedge angles that comprise the leading and trailing-edge surfaces of the two airfoils. Under ideal conditions, at the design Mach, the shockwaves generated by the leading-edge surfaces will cross before impinging directly on the apex of the opposite airfoil. Upon impingement at the apex of the airfoil, the flow is now turned out of itself, and no reflected shocks are generated. This is referred to as the wave cancellation effect. The wave cancellation effect occurs only at the specified design Mach as shown in figure 1.1. The intention of this design is to approximate a flat plate.

While this airfoil configuration does drastically reduce wave drag at the design Mach number, the same advantages are not seen at off-design conditions. At speeds greater than the design Mach, the shockwaves proceed to reflect beyond the central apex of the two airfoils. This causes a moderate increase in wave drag as the pressures on the rear surfaces of the airfoils are increased downstream of the reflected shockwaves. At speeds lower than the design Mach, a

detached shockwave (bow shock) will form near the leading edges. This phenomenon drastically increases wave drag and causes flow to choke within the inlet section of the biplane.

Additionally, a hysteresis phenomenon is present during acceleration and deceleration. On acceleration, unchoke conditions are delayed until speeds greater than the design Mach have been achieved. Once the flow is unchoked, it is possible to decelerate to the design Mach to achieve the wave cancellation effect. The mitigation of the flow choking phenomenon and reduction of the hysteresis region are the most critical design issues to address.

2.2.2 Flow Choking and Hysteresis

Early investigations suggested the possibility for detrimental flow choking to occur between the two airfoil surfaces of the Busemann biplane at speeds below the design Mach. This has been shown to drastically increase the wave drag generated as flow speed downstream of the bow shock is reduced to the subsonic range. The flow choking phenomenon was later confirmed experimentally in wind-tunnel analysis [9]. It was discovered in these early wind-tunnel investigations that, upon acceleration of flow to the design Mach of a Busemann biplane, the bow shock formed at the leading edges persisted. To the surprise of the researchers, the bow shock persisted well beyond the design Mach before ultimately being swallowed between the two surfaces at a speed greater than the design Mach number. It was then found that the more favorable oblique shock pattern persisted upon deceleration to the design Mach number. This is referred to as the hysteresis phenomenon due to the delayed cause and effect relationship seen between speed and shockwave formation.

Chapter 3 – Theoretical Approach

MATLAB will be used to calculate the Oblique Shock and Prandtl-Meyer relations as a theoretical framework. Through the application of the formulae and methods described above, flow variables are calculated around a given set of triangular biplane airfoils. The code is designed to be as versatile as possible, allowing for highly asymmetrical configurations. Additionally, as the goal of the theoretical calculator is to achieve rapid results, computational efficiency has been pursued in the architecture of the code.

This theoretical calculator determines whether a double triangular wedge biplane submerged in supersonic flow experiences peak elimination, as well as determine if the flow between the airfoils is decelerated to subsonic conditions at any point. Once flow variables are calculated, theoretical values for lift and drag coefficients are estimated.

3.1 Body Definition

The set of airfoils are defined by 10 variables:

Table 3. 1 – Design variables

Variable	Symbol
Lower Airfoil Angle of Attack	lAoA
Upper Airfoil Angle of Attack	uAoA
Lower Leading Edge Wedge Angle	LLA
Lower Trailing Edge Wedge Angle	LTA
Upper Leading Edge Wedge Angle	ULA
Upper Trailing Edge Wedge Angle	UTA
Chord Length of the Lower Airfoil	LC
Chord Length of the Upper Airfoil	UC
Vertical Offset Between the Leading Edges	VO
Horizontal Offset Between the Leading Edges	HO

These variables are used to generate the six spatial points that define the triangular wedge airfoils via trigonometric relations. The leading edge of the lower airfoil is always set to the origin point. The slopes of each line are stored for later use. These points are used to generate a structured array of symbolic surface functions. This array is titled Surfaces and contains the

functions, titles of the surfaces, and the initial and final x coordinates. The Surfaces array is ordered as follows:

Table 3. 2 – Surface definitions

Surface 1	Lower Flat Surface	LFS
Surface 2	Lower Leading Edge	LLE
Surface 3	Lower Trailing Edge	LTE
Surface 4	Upper Flat Surface	UFS
Surface 5	Upper Leading Edge	ULE
Surface 6	Upper Trailing Edge	UTE

These surfaces are then plotted, though it is not required to find a solution. Body validity is determined, ensuring that no surfaces intersect. The figure below shows a randomly generated pair of biplane airfoils.

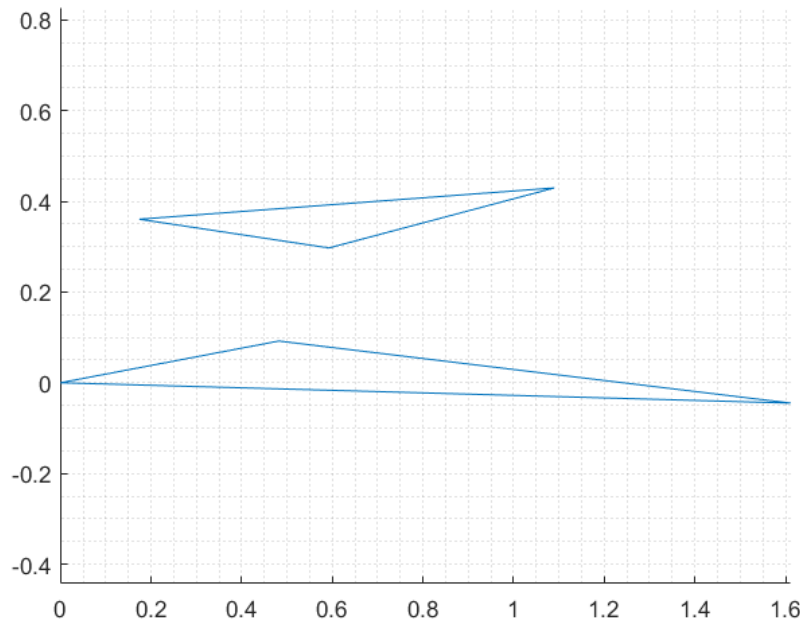


Figure 3. 1 – Example of a randomly generated supersonic biplane

3.2 Initial Wave Construction

Following the body generation, the initial waves are constructed. These are the four waves which emanate from the leading-edge points. The waves are constructed using shock-expansion theory as outlined in section 2.1.2., based on the surface angles, calculated from the surface slopes, and thus considering angle of attack of both airfoils. Flow variables upstream and downstream of the four perturbed regions are calculated and stored. This is sufficient to find the theoretical pressure ratios on the outer flat surfaces of the biplane. A new structured array called Waves is used to store certain values pertaining to the construction and display of the waves while vectors are sufficient to save flow variables. The first Waves value is assigned to freestream conditions. Waves 2 and 3 are those on the exterior of the biplane airfoil set. Waves 4

and 5 are those on the interior of the biplane set emanating from the lower and upper leading edges respectively. Symbolic formulas are once again used to define the wave location functions. The values saved in vectors are:

Table 3.3 – Flow vector definitions

Flow Value	Symbol	Vector Title
Beta Angle	β	B
Mach Number	M	M
Static Pressure Ratio, P	P/P_1	P
Static Temperature Ratio, T	T/T_1	T
Total Pressure Ratio, P0	P_0/P_{0_1}	P0
Total Temperature Ratio, T0	T_0/T_{0_1}	T0
Prandtl-Meyer function value, nu	ν	nu
Mach Angle, mu	μ	mu

3.3 Fore Section Shock Interactions

The shock-shock interactions between the two opposing leading-edge sections are calculated using Oblique-Shock Theory. The first and subsequent points of intersection between the left and right running shockwaves are calculated by setting the wave location functions equal and solving for x. This value is stored as the terminating x-coordinate in the Waves structure for the corresponding Waves.

Following this, opposite family shock interactions are calculated with constructed OFSI function. The OFSI function performs the iterative guess-and-check process described in Chapter 2, Section 2.1.2. Initially, the slip angle, ϕ , is set to 0. Upon calculating the downstream flow properties from the two refracted waves, the pressure ratios are compared. As it would be computationally expensive to try to achieve a perfect match of pressure coefficients, the comparison is made against a predefined tolerance value, PhiAccuracy. If the absolute value of the difference between the pressure ratios of the right and left running refracted shocks are less than PhiAccuracy, OFSI returns the downstream flow values as well as the necessary Waves values. If the difference is greater, the slip angle is adjusted. If the pressure ratio downstream of the right-running refracted wave is greater than that of the left-running refracted wave, the slip angle is increased, and vice versa. The amount to which the slip angle is increased or decreased is reduced with each iteration. Through experimentation, it was determined that a PhiAccuracy value of 0.00001 produces accurate downstream values while preserving the low computation time.

Once the refracted shocks have been solved, the subsequent reflected shocks, if they exist, are calculated. This process is similar to the refracted shocks. The point of impingement between the refracted shocks and the corresponding leading-edge surface are found by setting the

surface function equal to the wave location function and solving for x . Flow values downstream of the reflected shock are calculated as described in Chapter 2 and saved. All flow ratios are calculated in reference to the freestream.

To capture the peak elimination phenomenon, the distance between the impingement points and the central apex of the airfoil in consideration is compared to a variable `PeakEliminationProximity`. If the point of impingement is close enough to the central apex, a one (1) is stored in the pseudo-logical `Waves` array variable `peaked`. If either one of the refracted waves is found to continue beyond the central apex of a foil, a value of zero (0) is given to the wave and in the leading-edge shock interaction, calculations are concluded. All other waves receive no value in the `peaked` variable.

Shockwaves that either emanate from or impinge upon the lower airfoil are assigned an even numbered wave designation number, while shockwaves that emanate from or impinge upon the upper airfoil are assigned odd wave designation numbers. The figure below gives an example of the refracted and reflected shocks generated as well as their corresponding wave designation number for an asymmetrical biplane with zero lower angle of attack, upper angle of attack, and horizontal offset, submerged in Mach 2 flow.

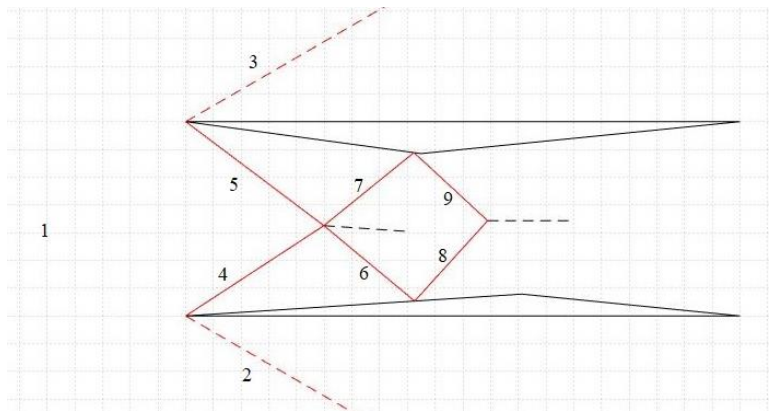


Figure 3. 2 – Example of fore shock interactions with wave designations

The values stored in the Waves structured array are:

Table 3. 4 – Waves structured array variable definitions

Wave Value	Value title	Definition
Spatial function	F	Linear function for the y-coordinate of the wave at a given x
X limits	X	The x limits of the wave as defined by the originating point of the wave and the final point of the linear wave
Flow Angle	flowAngle	The angle of the flow relative to the freestream
Wave Type	Type	Stores the type of the wave: shock, expansion or sonic
Wave Family	Running	Stores the family of the wave: right running or left running
Peak elimination pseudo-logical	Peaked	Holder value that simultaneously identifies the final shock waves and identifies if the final wave experiences peak elimination.

3.4 Aft-section Shock-Expansion Interaction

Once the fore-section shock-shock interactions are solved, the aft-section shock-expansion interaction section begins. Considering the geometry, it is obvious that there is no valid configuration which results in shockwaves forming from the central apex of the triangular section biplane airfoils. The flow is always turned outward at these points and thus there will always be Prandtl-Meyer expansion fans originating from these points. Expansion fans, as described in Chapter 2, are made up of an infinite number of Mach waves. However, as that is not feasible to display or calculate, a variable FanDensity is used to specify the number of Mach waves in consideration.

A new structured array called Char is used to save wave variables. The upstream values used in the calculation of the expansion fans are determined through inspection of the peaked variable in the Waves array. If peak elimination is not observed, the final shockwaves from the fore section are entered into the Char array. If peak elimination is observed, upstream conditions are taken from that downstream of the corresponding refracted shock, as no reflected shock is generated, and no shockwaves are entered into the Char array. If no peak elimination occurs, the final shockwave or shockwaves are imported into the method of characteristics section.

Once the initial expansion fans have been calculated, further calculation based on the method of characteristics is implemented to find more accurate locations of impingement between the aft surfaces and the shock and expansion waves contained within the aft section of the biplane. The downstream flow Mach and flow angle of all refracted and subsequently reflected waves are estimated using the methods outlined in section 2.1.3. This allows for a quick visualization of the flow through the aft section of the biplane. As this theoretical calculation is just needed for initial inspection, only one iteration of the method of characteristics is employed

to determine if at any point between the biplane surfaces, the flow is likely to be reduced to subsonic conditions.

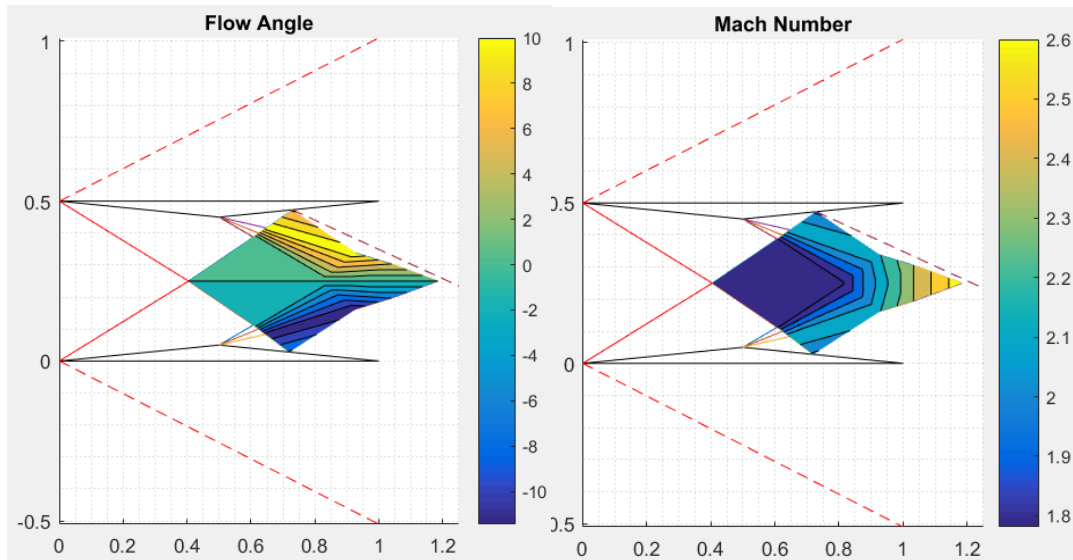


Figure 3. 3 - Visualization of the flow through the aft section of the biplane

Figure 3.3 below shows a comparison between calculated MATLAB flow field (red and blue dotted lines) against CFD results from reference 5 of a Busemann biplane with a design Mach of 1.7 at Mach 2.18.

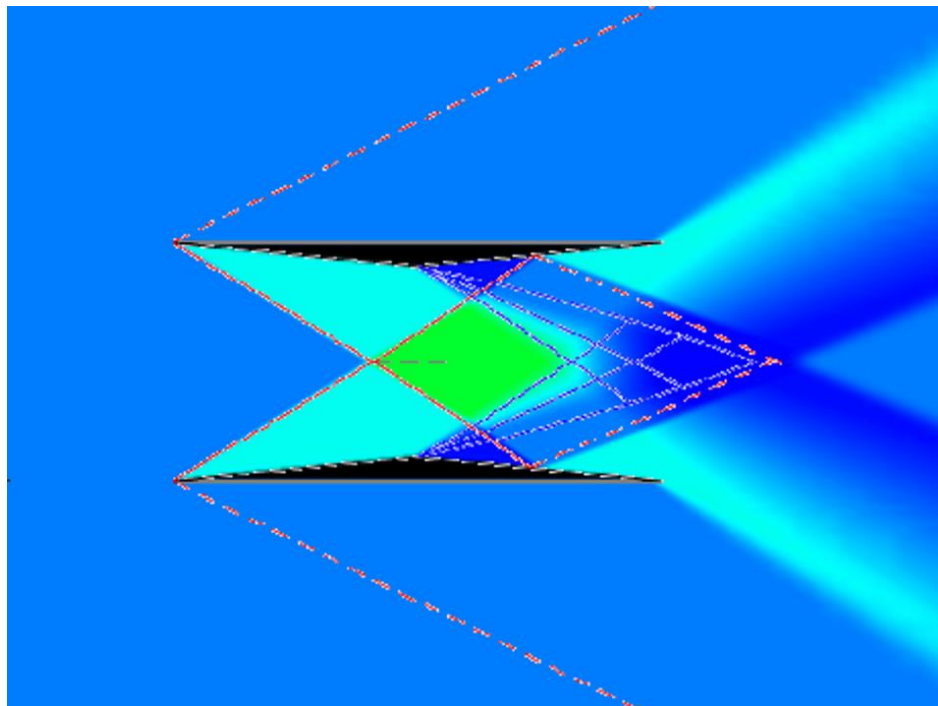


Figure 3. 4 - Comparison between predicted theoretical flow field and historical CFD

3.5 Theoretical Flow Values and Coefficients

The theoretical lift and drag coefficients are calculated based on the pressure ratios as described in Chapter 2. This is done piecewise for each surface. The lower (surface 1) and upper (surface 4) surface calculations are simple, as those experience no wave interactions. The normalization chord lengths used are those which correspond to the airfoil in consideration, e.g., the formula used to find the lift coefficient on surface 1 is:

$$c_{lS1} = lc \left(\frac{P_2}{P_1} - 1 \right) \cos(\text{atand}(LSm)) \cdot \frac{2}{\gamma M_1^2 lc} \quad (3.1)$$

and the formula used to find the lift coefficient on surface 4 is:

$$c_{lS4} = uc \cdot - \left(\frac{P_3}{P_1} - 1 \right) \cos(\text{atan}(USm)) \cdot \frac{2}{\gamma M_1^2 uc} \quad (3.2)$$

Both the leading-edge surfaces, surfaces 2 and 5, must be further delineated into sections corresponding to the locations of shock impingement. The length of the section is determined by the origin points of reflected waves. The pressure ratios used are those downstream of the reflected waves with reference to the freestream.

The lower and upper trailing surfaces, surfaces 3 and 6 respectively, must be divided in the same manner as surfaces 2 and 5. A vector of points of impingement is created to divide the surface into sections. For each section, the lift and drag coefficients are calculated as well as the pressure ratio of the next section. If the aft impinging wave is a shockwave, the next section pressure ratio is calculated using entropic oblique shock relations. If the next section impinging wave is an expansion wave, the next section pressure ratio is calculated through the isentropic relations. The formulae employed are outlined in section 2.1.2.

3.6 Limitations

This theoretical calculation suffers from certain limitations due to the nature of the formulas behind Shock-Expansion theory, as well as code-based limitations due to the sequential nature of MATLAB.

3.6.1 Limitations Within Shock-Expansion Theory

The primary limitation within shock-expansion theory is that flow must be supersonic. If at any point, the flow speed is reduced below a Mach number of 1, no reliable results may be found through the implementation of shock-expansion theory. As such, it is not possible to capture the amount of hysteresis a given biplane design will experience. Lastly, this theoretical framework does not take viscosity into consideration.

3.6.2 Limitations Within the Coding Methodology

The limitations within the MATLAB calculation of theoretical coefficients exist due to certain tradeoffs between coding robustness and preserving computational time. Currently, no solutions are given for cases wherein leading-edge shocks pass in front of the opposing foil or cases in which either airfoil is angled such that an expansion fan forms in the fore-section, therefore there must be shock-shock interactions within the fore-section for a solution to be found. Currently, no formulation for shock/expansion generation at the trailing edge has been implemented, so if the trailing edge waves from one foil interact with the opposing foil, this would not be taken into consideration.

As previously stated, it is prohibitively expensive to achieve perfect agreement between pressure ratios downstream of opposite family shock interactions. Similarly, an amount of approximation is inherent in the calculation of the method of characteristics section. The degree of accuracy to which the method of characteristics calculates the flow field is dependent on the variable fanDensity. A benchmark study will be conducted to determine an appropriate value to use for this variable which preserves computation time while achieving accurate results.

Chapter 4 – Computational Approach

The CFD software, ANSYS Fluent, will be used to simulate flow around various biplanes at different conditions and to further verify and validate the theoretical calculation of aerodynamic coefficients via MATLAB. This will also be necessary to ascertain the level of hysteresis experienced with a given biplane design.

4.1 Computational Domain Definition

The computational domain employed is a limited farfield set 3 meters away from the biplane in the x and y directions. The domain is split into ten faces. Each split is cut horizontally and vertically from each of the vertexes. Internal to the biplane set, the split is done between the leading edges, trailing edges, and central apex, regardless of horizontal offset or other asymmetries. Biplane airfoil shape is defined similar to the methods used in the theoretical MATLAB calculation.

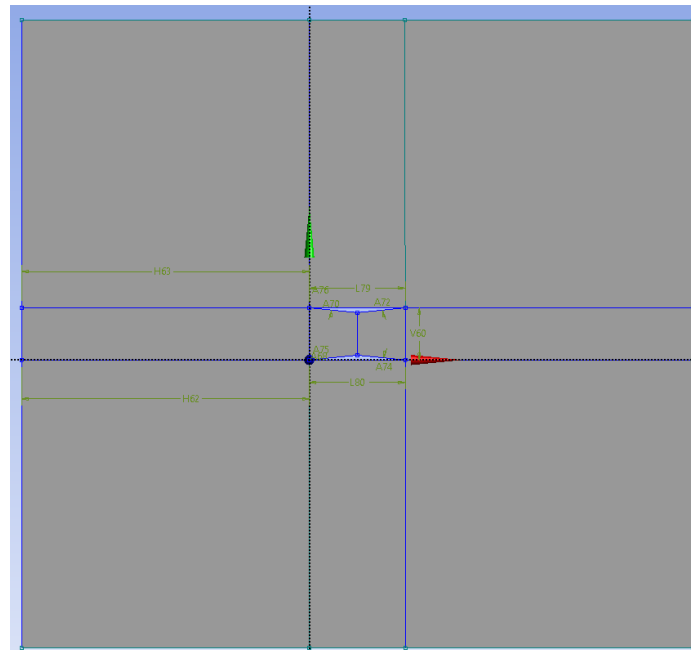


Figure 4. 1 – Farfield employed

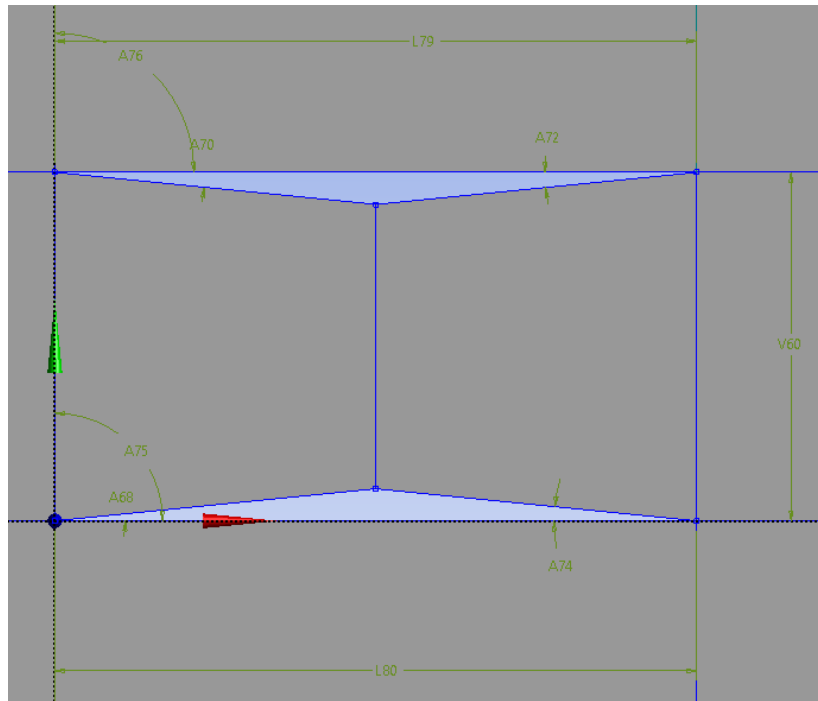


Figure 4. 2 – Symmetrical biplane configuration with dimensions

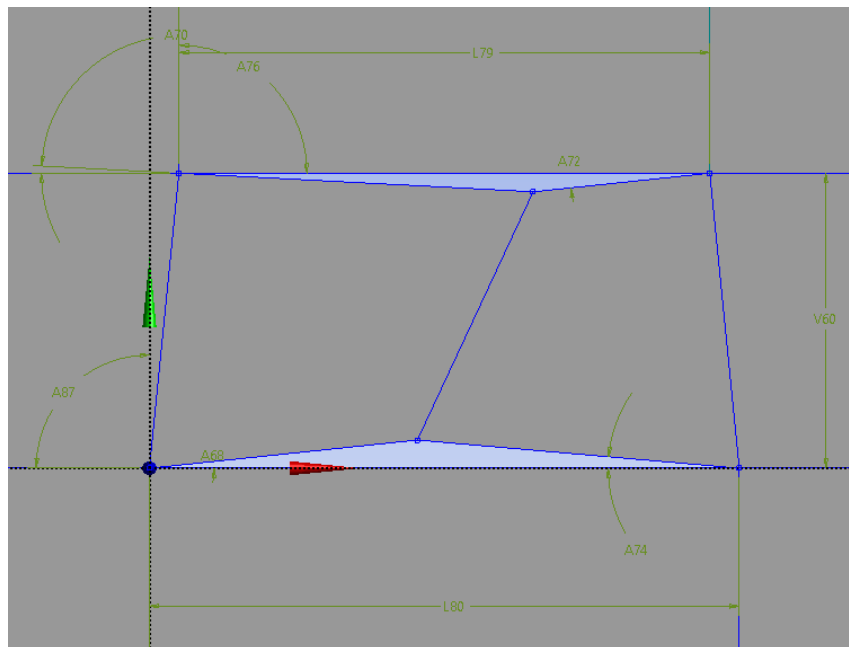


Figure 4. 3 – Asymmetrical biplane configuration with dimensions

4.2 Grid Generation

A structured grid is employed through the computational domain. The mesh is generated with 161,800 elements. Careful consideration has been taken with edge spacing and biasing to avoid having low quality elements near the biplane surfaces while maintaining fine enough detail to capture boundary layer effects.

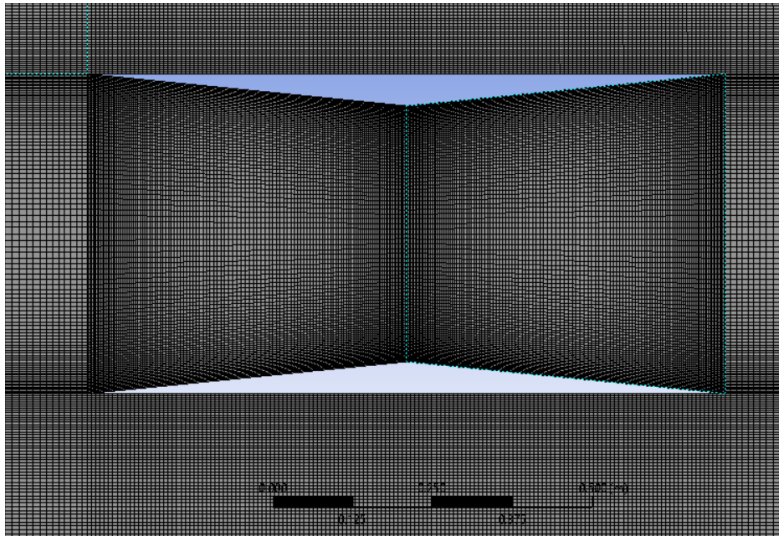


Figure 4. 4 – Near grid around symmetrical biplane set

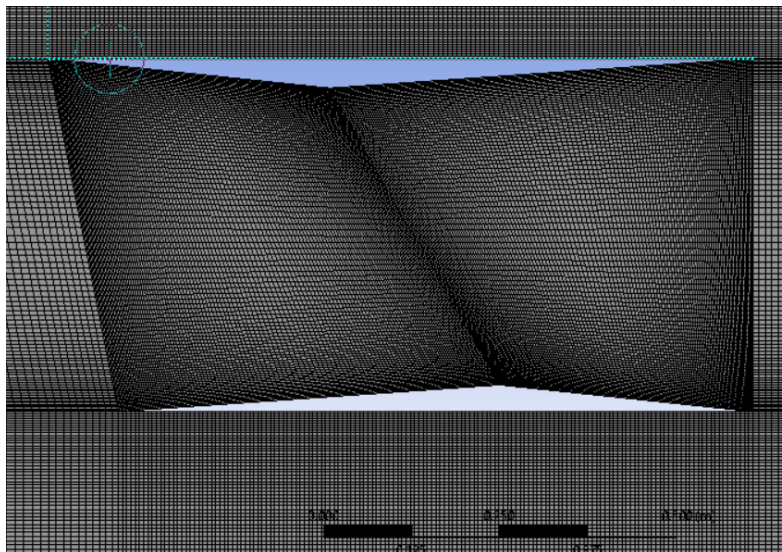


Figure 4. 5 – Near grid around asymmetrical biplane set

4.3 Fluent Settings

Within the benchmark study, ANSYS Fluent simulations will be conducted using multiple flow types, namely:

- Inviscid
- Viscous Laminar
- Viscous Turbulent

The turbulence model used is Spalart-Allmaras with curvature and corner flow corrections. All models are run density based employing the energy equation. The fluid used is air with density determined through the ideal gas relations. Thermal conductivity is determined via kinetic theory. Viscosity, for those models that employ it, is determined through the

Sutherland’s law. All other fluid quantities are kept at their default unless otherwise specified in the benchmark studies.

The boundary conditions are set as a pressure farfield with a gauge pressure of 101325 pascals and the default temperature of $288.16^{\circ} K$. The foil wall is set to stationary with the same default temperature. The roughness is set to standard, and the no-slip condition is employed. Reference values are computed from the farfield.

The solution methods employed are implicitly based with higher order terms relaxed. Spatial discretization is done using the green-gauss node-based method. All flow and turbulence discretization are conducted with the third order MUSCL scheme. Transient formulation is first order implicit.

Lift coefficient, drag coefficient, and pitching moment coefficients are calculated using the standard methods. Lift-to-drag ratio is also defined and solved for. Convergence conditions have been lowered to at least $1E-4$. Hybrid initialization is employed. The calculation is run for 2000 iterations in a steady state configuration. Convergence tends to be achieved in around 45 minutes utilizing 3 CPU threads and GPU acceleration.

4.4 Grid Independence and Verification Against Historical Data

A grid independence study is first conducted against historical data. Previous studies have focused on a baseline biplane corresponding to a 10% diamond airfoil with a design Mach of 1.7. This translates to wedge angles of 5.71° and a spacing of 0.5m between the leading edges. At Mach 1.7, this design has a drag coefficient of approximately 0.0021 when inviscid flow is used [5].

Using the above stated mesh in the inviscid mode, a drag coefficient of 0.0020 is found. This already shows good agreement between historical data both in drag coefficient and in the overall flow field shown below. The differences in the color scheme are likely due to differences in software.

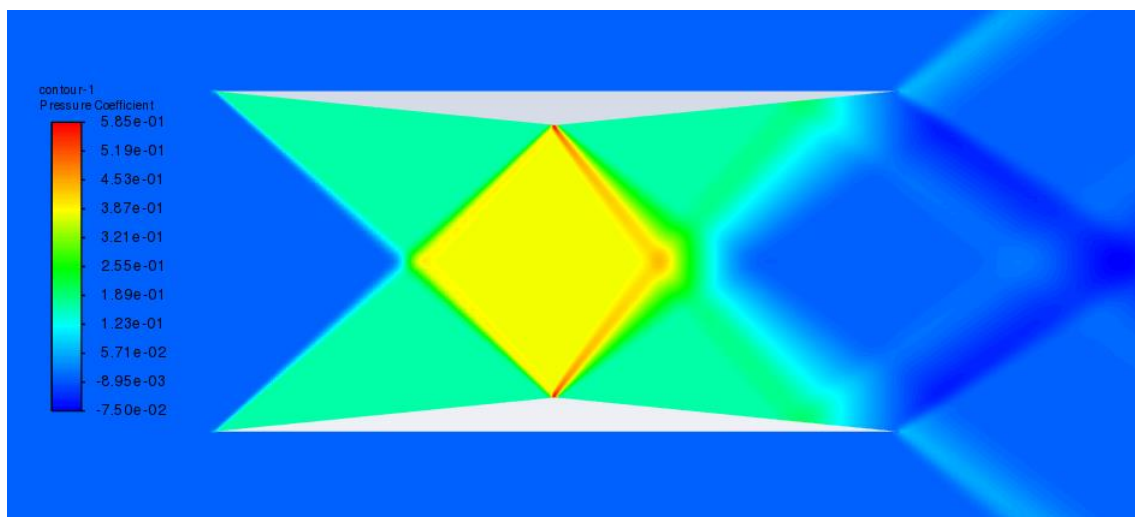


Figure 4. 6 – Pressure contours from ANSYS

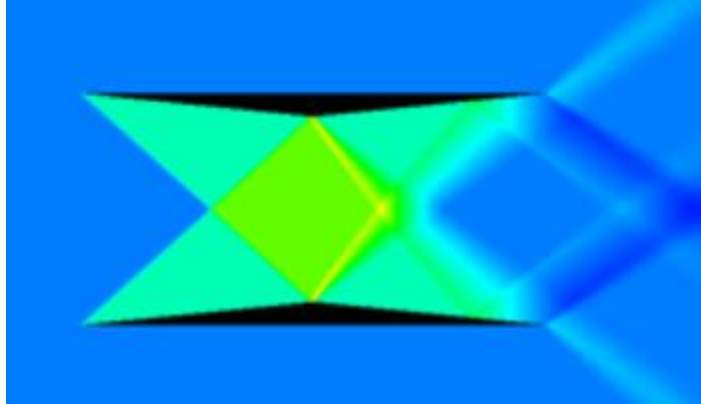


Figure 4.7 – Pressure contours from historical data generated in UPACS [5]

Further testing is conducted on grid independence with element quantities of 189,200, 152,000, 126,360, and 87,680. Cell spacing was reduced by roughly one-half to achieve the element quantity of 87,680. This did not converge to a solution. Further reductions in accuracy were observed in solutions with each reduction in element quantity. Thus, moving forward, an element quantity of 161,800 will be used.

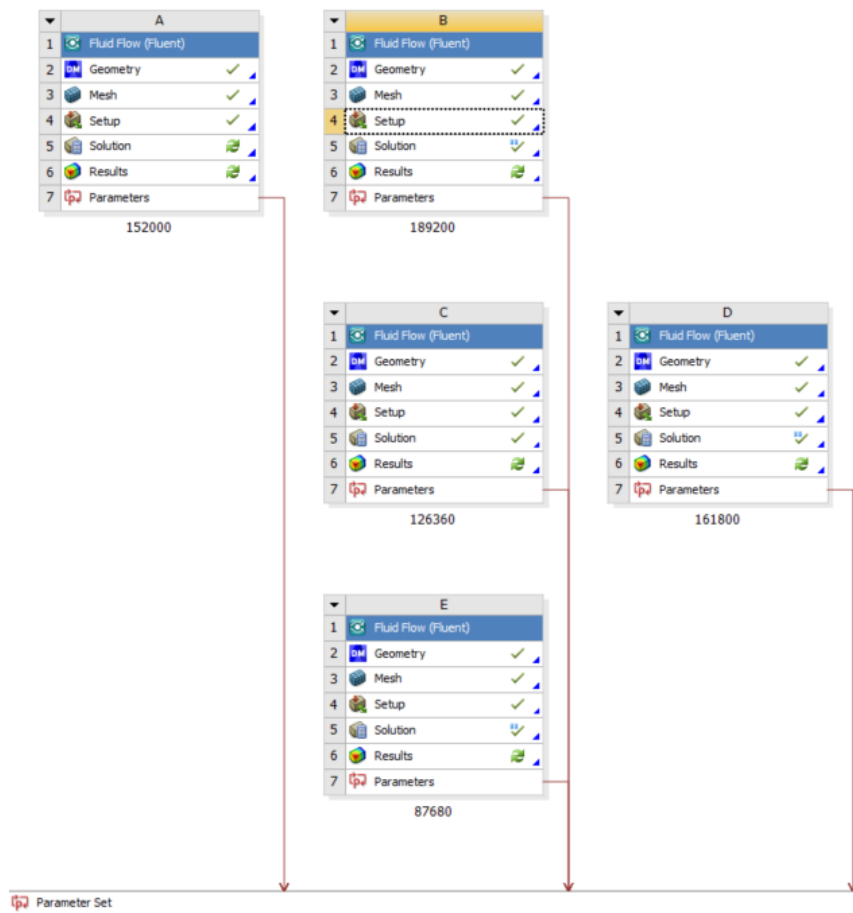


Figure 4.8 – Grid independence study

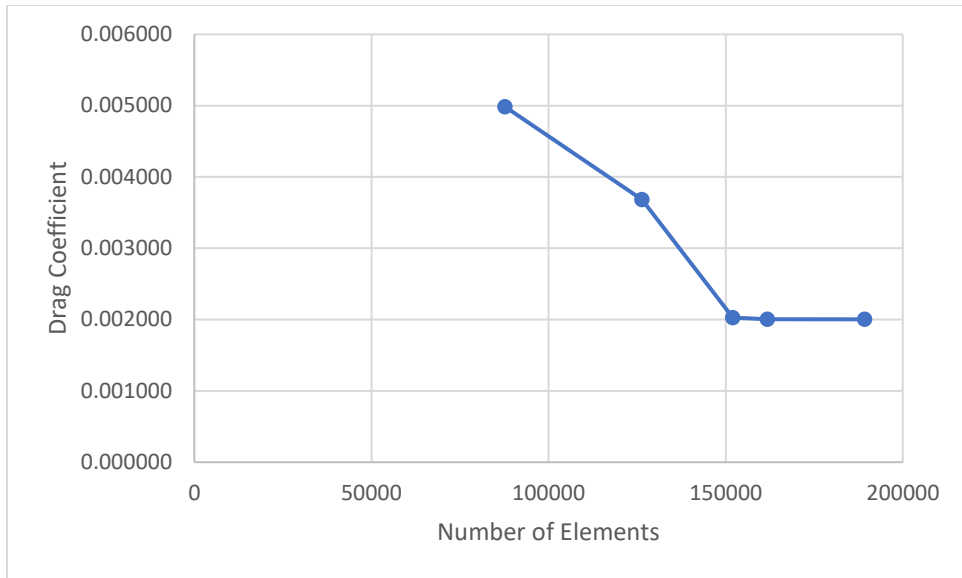


Figure 4. 9 – Results from grid independence study

Chapter 5 - Verification and Validation

5.1 Verification Against Historical Data

The paper *A study of Busemann-type Biplane for Avoiding Choked Flow* by Yamashita et al. was a preliminary investigation into the capabilities of Busemann biplanes [5]. This investigation was conducted primarily using an inviscid CFD solver. As such, the values presented in the paper are useful as a means of verifying the functionality of this theoretical calculator.

5.1.1 Verification of Preliminary Wave Calculation

As a preliminary step, it is useful to verify the preliminary wave values within the theoretical calculator. This is achieved by setting the horizontal offset distance between the leading edges of the biplane airfoils to zero (0) and setting the lower and upper angles of attack equal to each other. This effectively approximates a diamond airfoil. As the diamond airfoil is often used as a point of comparison for the functionality of a Busemann biplane, this tool will be useful later. Theoretical coefficients may be calculated by removing the opposite family shock interaction section and the method of characteristic sections. Using MATLAB, it is simple to run this for a range of Mach numbers. Plotting this against the data presented in reference 5 shows good agreement between drag coefficient values achieved via MATLAB. In the figure below, theoretical drag coefficients calculated are plotted in green while the grey line represents the drag coefficient values achieved through CFD.

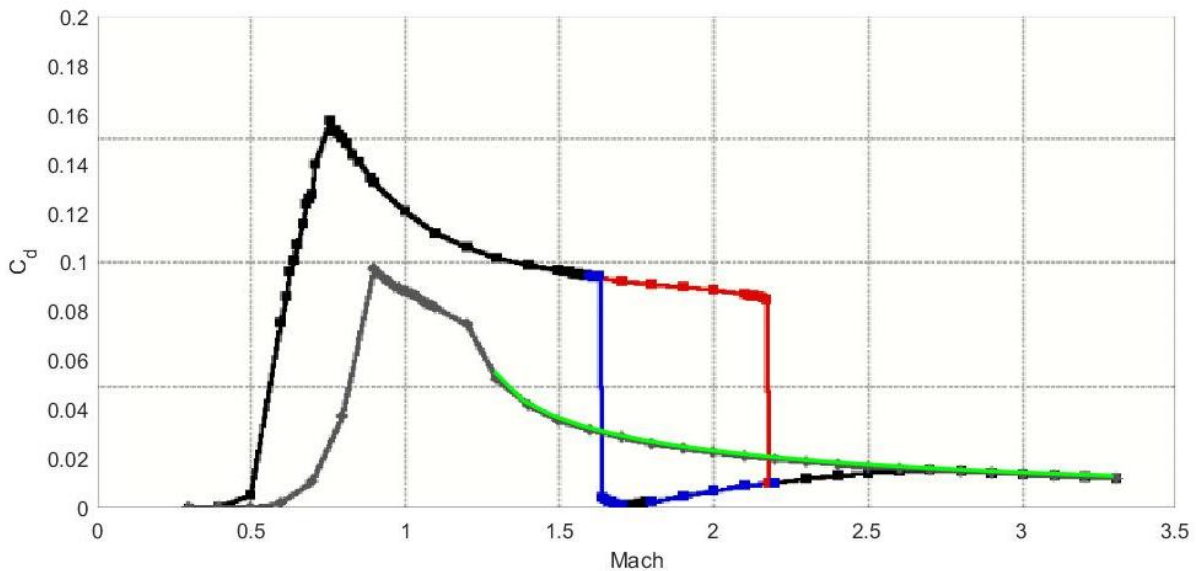


Figure 5. 1 – Preliminary wave validation

Further validation can be done by comparing the lift coefficients calculated to those presented in the NACA technical report #1316 [1]. All calculations in this report were conducted without the aid of CFD and as such, this report was also inviscid and took a number of additional approximations in their calculations. Despite this, plotting the lift-to-drag ratio against those presented in the NACA technical report again shows a high degree of corroboration with the theoretical calculator and historical data and methods. Slight discrepancies exist, likely due to approximations made.

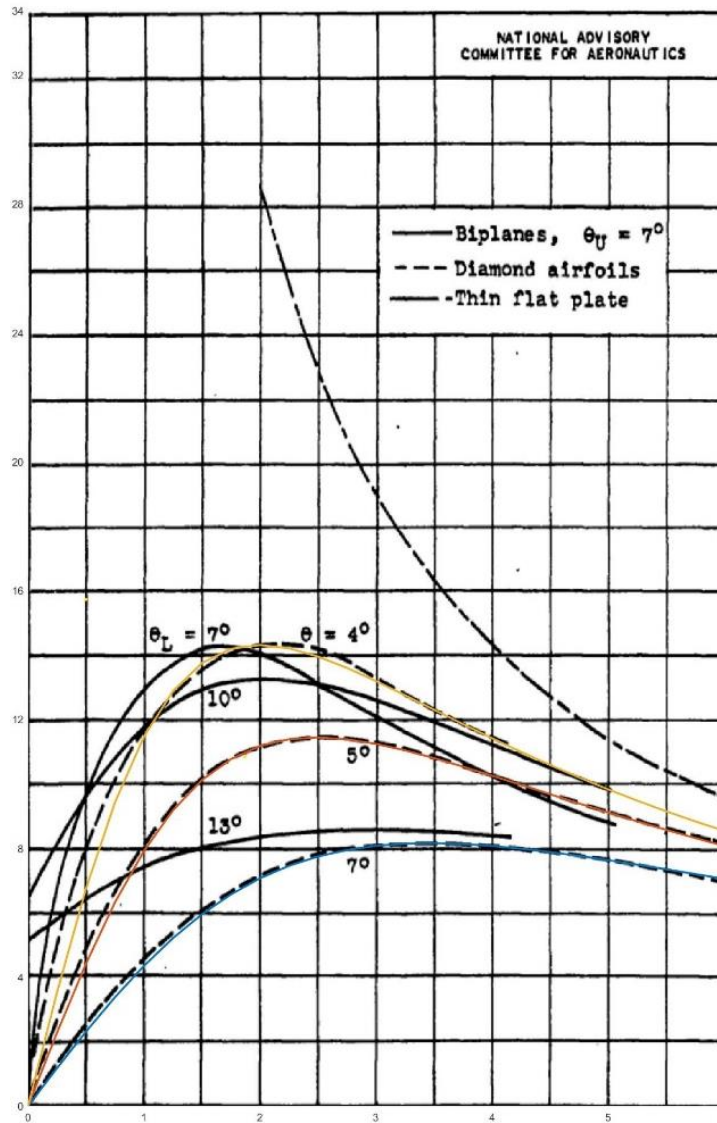


Figure 5. 2 – L/D vs AoA validation of initial wave formulation

5.2 Baseline Benchmark Studies Between Theory and CFD

Benchmark studies will be performed to verify and validate the theoretical calculator. Two designs will be taken into consideration. The first design will be referred to as Baseline 1. It is the baseline used in much of the historical data, that being, a symmetrical biplane with zero staggering, wedge thicknesses of 0.05 meters, and a horizontal spacing of 0.5 meters. The

purpose of Baseline 1 is to continue the comparison against historical data, as well as inspect the validity of the formulation of the peak elimination phenomenon. The second design taken into consideration will be referred to as Baseline 2. This design is an asymmetric configuration with zero stagger.

The purpose of Baseline 2 is to inspect the validity of the coefficient formulation around the internal surfaces. The exact values of Baseline 1 and Baseline 2 are compared in table 5.1 below.

Table 5. 1 - Baseline 1 and 2 value comparison

Attribute	Baseline 1	Baseline 2
Lower Leading Angle (LLA)	5.7106°	6°
Lower Trailing Angle (LTA)	5.7106°	4°
Upper Leading Angle (ULA)	5.7106°	4°
Upper Trailing Angle (UTA)	5.7106°	6°
Lower Chord Length (lc)	1 [m]	1 [m]
Upper Chord Length (uc)	1 [m]	1 [m]
Vertical Offset (vo)	.5 [m]	.5 [m]
Horizontal Offset (ho)	0 [m]	0 [m]

5.2.1 Baseline Benchmark Study Between Theory and CFD for Viscous Models

The theoretical calculator will be benchmarked against CFD results for Baseline 1 and Baseline 2 at Mach numbers of 1.7 and 2. In the theoretical calculator, an arbitrary value of 15 is used for the variable fanDensity. Additionally, both designs will be run with the viscous models of inviscid, viscous laminar, and viscous turbulent. The ANSYS setup is shown in Figure 5.3 below. The percent differences between the lift and drag coefficients found via MATLAB and ANSYS are calculated to highlight areas where the theoretical calculator performs poorly.

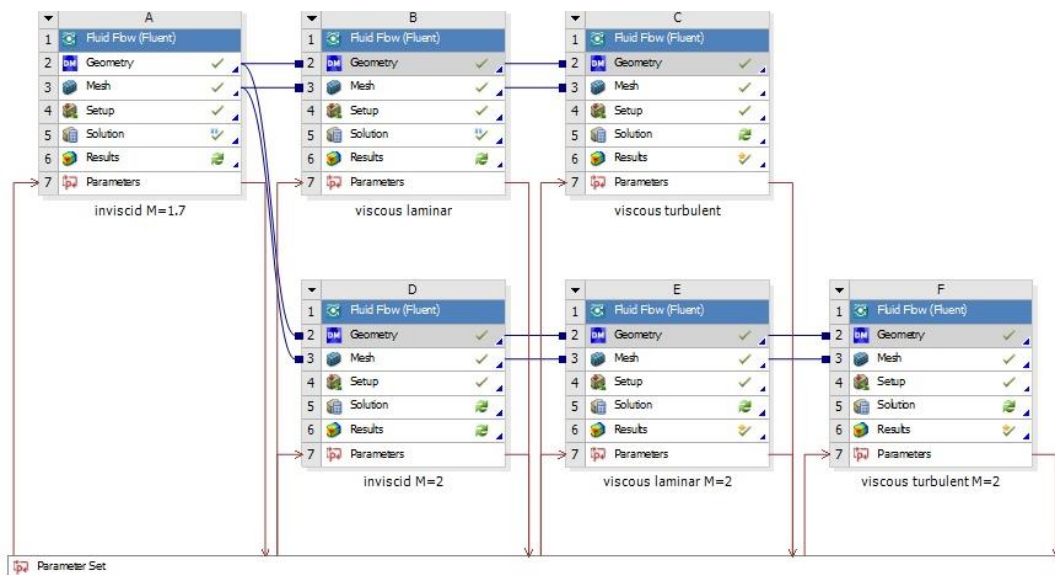


Figure 5. 3 – ANSYS set up

Figures 5.4 and 5.5 provide a graphical display of the comparison of data between MATLAB and ANSYS for Baseline 1 at Mach 1.7. Results show agreement between the characteristic mesh predicted through MATLAB and the pressure ratios calculated through ANSYS. The pressure ratios shown in ANSYS are calculated by dividing the static pressure by the freestream static pressure, 101,325 Pa. It should be noted that the effects of the dashed characteristic lines are not taken into consideration when calculating the theoretical drag, resulting in higher predicted pressure ratios, thus reducing the drag predicted in MATLAB. The pressure ratio at the trailing edge calculated in ANSYS was approximately 1.017 while the pressure ratio at the trailing edge calculated in MATLAB was 1.241.

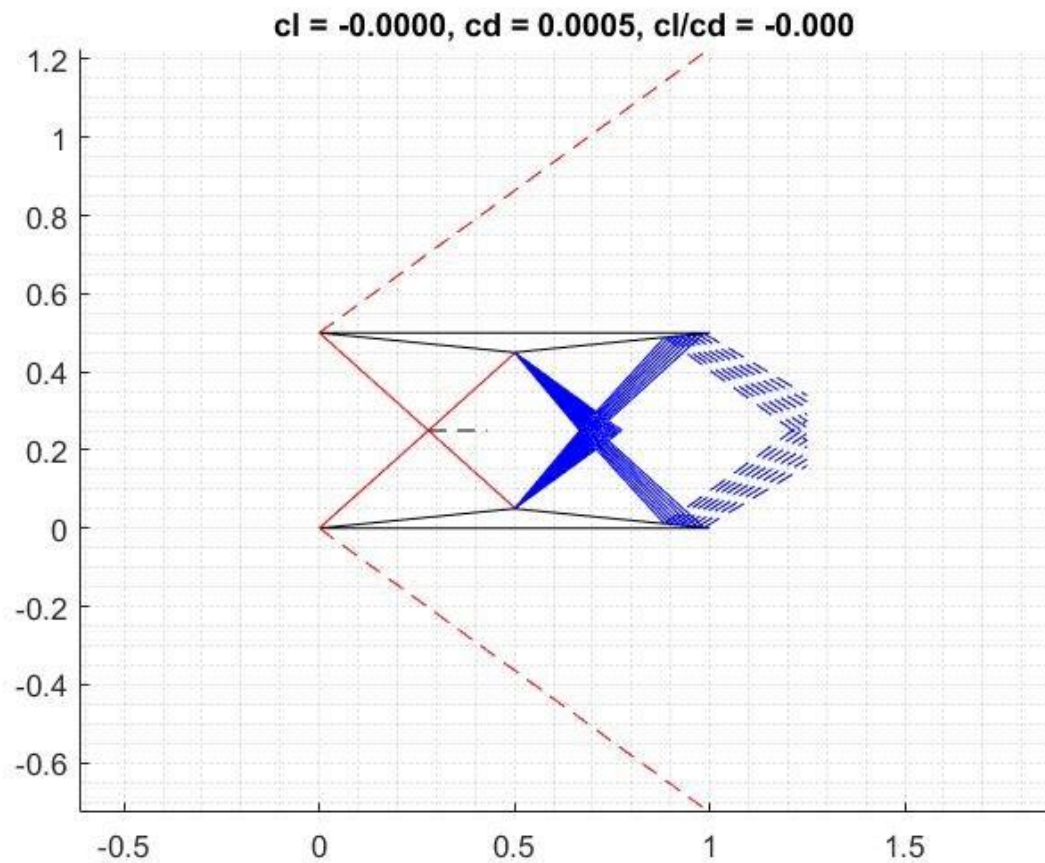


Figure 5. 4 - MATLAB graphical display for Mach 1.7

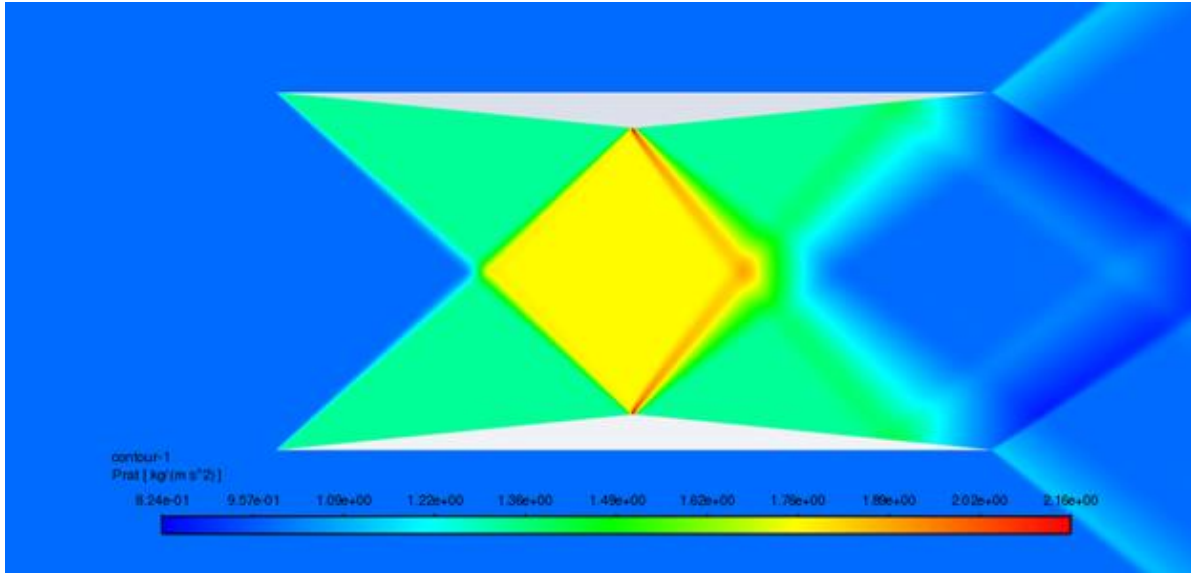


Figure 5. 5 - ANSYS graphical display for Mach 1.7

Tables 5.2 through 5.5 demonstrate the differences in results between MATLAB and ANSYS for all Baseline 1 considerations. For the symmetric configuration, Baseline 1 lift coefficient formulation was handled well, adequately cancelling the positive and negative lift generated on the upper and lower airfoils. The drag coefficient estimated through MATLAB was considerably lower than shown through CFD. The results with the greatest deviation from CFD were shown on the upper and lower trailing edges. This was seen for both Mach 1.7 and Mach 2.

Table 5. 2 - Baseline 1, Mach 1.7, lift & drag coefficient

Baseline 1	MATLAB	ANSYS Fluent			% difference		
Mach = 1.7	Theoretical	Inviscid	Viscous Laminar	Viscous Turbulent	Inviscid	Viscous Laminar	Viscous Turbulent
Lift Coefficient	0.0000	0.0000	0.0000	0.0000	~0%	~0%	~0%
Drag Coefficient	0.0005	0.0020	0.0025	0.0100	75%	80%	95%

Table 5. 3 – Baseline 1, Mach 1.7, breakdown of surfaces

Baseline 1	Theoretical		CFD - Inviscid		% difference	
M = 1.7	Lift	Drag	Lift	Drag	Lift	Drag
LFS	0.0000	0.0000	0.0000	0.0000	~0%	~0%
LLE	-0.0821	0.0082	-0.0847	0.0085	3%	3%
LTE	-0.0796	-0.0080	-0.0748	-0.0075	6%	6%
UFS	0.0000	0.0000	0.0000	0.0000	~0%	~0%
ULE	0.0821	0.0082	0.0846	0.0085	3%	3%
UTE	0.0796	-0.0080	0.0749	-0.0075	6%	6%
Total	0.0000	0.0005	0.0000	0.0020	85%	74%

Table 5.4 – Baseline 1, Mach 2, lift & drag coefficient

Baseline 1	MATLAB	ANSYS Fluent			% difference		
Mach = 2	Theoretical	Inviscid	Viscous Laminar	Viscous Turbulent	Inviscid	Viscous Laminar	Viscous Turbulent
Lift Coefficient	0.0000	0.0000	0.0000	0.0000	~0%	~0%	~0%
Drag Coefficient	0.0131	0.0080	0.0084	0.0148	64%	56%	12%

Table 5.5 – Baseline 1, Mach 2, breakdown of surfaces

Baseline 1	Theoretical		CFD - Inviscid		% difference	
	Lift	Drag	Lift	Drag	Lift	Drag
LFS	0.0000	0.0000	0.0000	0.0000	~0%	~0%
LLE	-0.0654	0.0065	-0.0653	0.0065	0%	0%
LTE	-0.0387	-0.0039	-0.0256	-0.0026	51%	51%
UFS	0.0000	0.0000	0.0000	0.0000	~0%	~0%
ULE	0.0654	0.0065	0.0653	0.0065	0%	0%
UTE	0.0387	0.0039	0.0256	-0.0026	51%	251%
Total	0.0000	0.0131	0.0000	0.0080	~0%	64%

Figures 5.6 and 5.7 demonstrate differences between MATLAB and ANSYS for Baseline 2 at Mach 1. Similar to Baseline 1, the results indicated agreement between the characteristic mesh generated in MATLAB and the pressure ratios calculated in ANSYS. The greatest visual discrepancy between these two results exists on the downstream left running reflected shock wave on the lower surface. This is, again, likely because of the reflected shock upstream of that wave were not taken into consideration. The pressure ratios at the upper and lower trailing edges calculated through ANSYS were approximately 0.7749 and 1.492 respectively, while the pressure ratios for the same points calculated through MATLAB were 1.163 and 1.489.

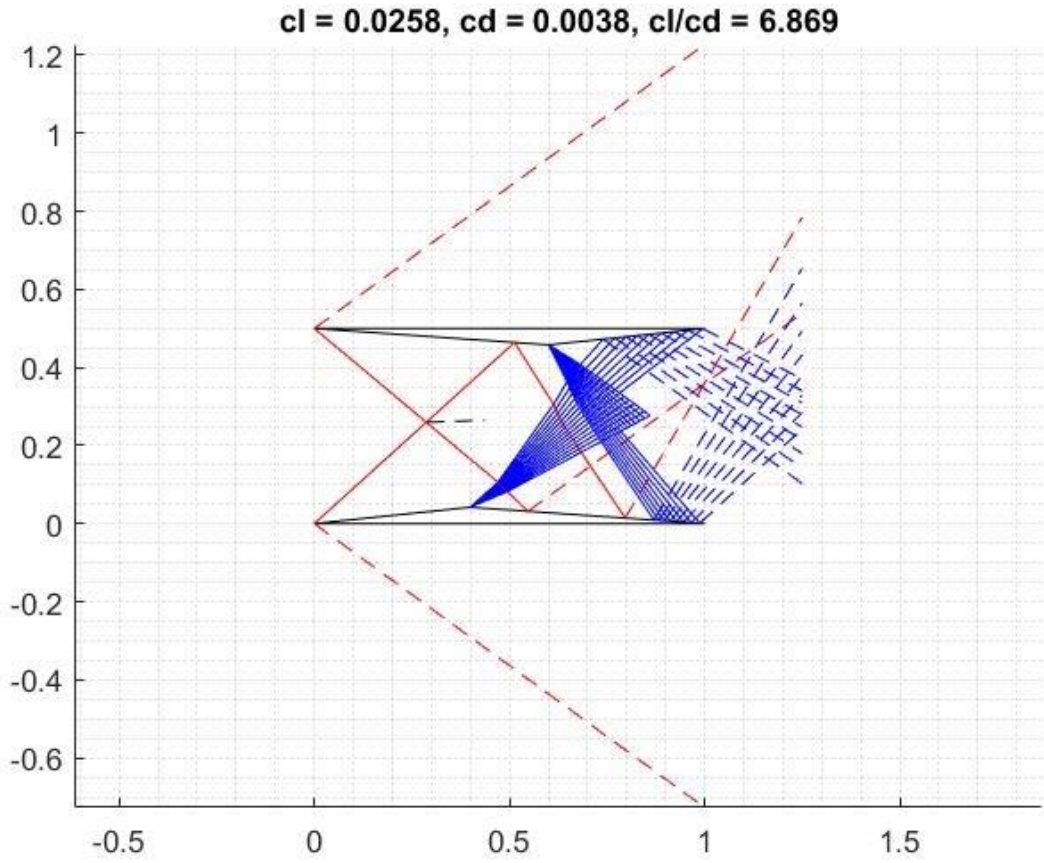


Figure 5. 6 - MATLAB graphical display of baseline 2 at Mach 1

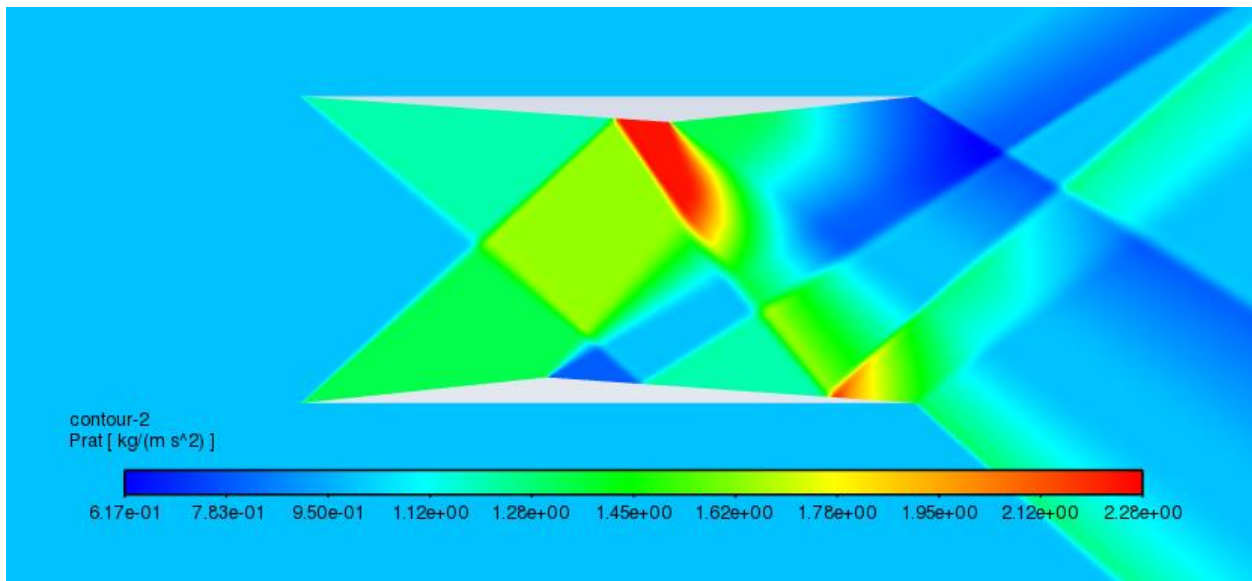


Figure 5. 7 - ANSYS graphical display of baseline 2 at Mach 1

Tables 5.6 through 5.9 below show the differences in all results between MATLAB and ANSYS for Baseline 2, the asymmetric configuration. Drag calculations were accurate to CFD for inviscid and viscous laminar for both Mach 1.7 and Mach 2. The lift coefficient calculation showed a dramatic difference between the CFD simulation and theoretical calculator. The primary difference was shown on the upper and lower trailing edge surfaces. The lower trailing surface at Mach 1.7 achieved almost perfect agreement with inviscid CFD results.

Table 5. 6 – Baseline 2, Mach 1.7, lift & drag coefficient

Baseline 2	MATLAB	ANSYS Fluent			% difference		
Mach = 1.7	Theoretical	Inviscid	Viscous Laminar	Viscous Turbulent	Inviscid	Viscous Laminar	Viscous Turbulent
Lift Coefficient	0.0262	-0.0025	-0.0037	-0.0099	1130%	816%	364%
Drag Coefficient	0.0037	0.0062	0.0070	0.0142	42%	48%	74%

Table 5. 7 – Baseline 2, Mach 1.7, breakdown of surfaces

Baseline 2	Theoretical		CFD - Inviscid		% difference	
M = 1.7	Lift	Drag	Lift	Drag	Lift	Drag
LFS	0.0000	0.0000	2.84E-05	1.31E-18	~0%	~0%
LLE	-0.0694	0.0073	-0.06667	0.007007	4%	4%
LTE	-0.0743	-0.0052	-0.07404	-0.005178	0%	0%
UFS	0.0000	0.0000	-1.84E-06	0	~0%	~0%
ULE	0.1108	0.0078	0.108173	0.007564	2%	2%
UTE	0.0590	-0.0062	0.0300	-0.0032	97%	97%
Total	0.0262	0.0037	-0.0025	0.0062	1130%	42%

Table 5. 8 – Baseline 2, Mach 2, lift & drag coefficient

Baseline 2	MATLAB	ANSYS Fluent			% difference		
Mach = 2	Theoretical	Inviscid	Viscous Laminar	Viscous Turbulent	Inviscid	Viscous Laminar	Viscous Turbulent
Lift Coefficient	0.0468	0.0350	0.0351	0.0354	34%	33%	32%
Drag Coefficient	0.0036	0.0057	0.0061	0.0127	37%	41%	72%

Table 5. 9 – Baseline 2, Mach 2, breakdown of surfaces

Baseline 2	Theoretical		CFD - Inviscid		% difference	
M = 2	Lift	Drag	Lift	Drag	Lift	Drag
LFS	0.0000	0.0000	0.0000	0.0000	~0%	~0%
LLE	-0.0552	0.0058	-0.0552	0.0058	0%	0%
LTE	-0.0042	-0.0003	0.0006	0.0000	853%	60%
UFS	0.0000	0.0000	0.0000	0.0000	~0%	0%
ULE	0.0529	0.0037	0.0529	0.0037	0%	0%
UTE	0.0534	-0.0056	0.0368	-0.0039	45%	5%
Total	0.0468	0.0036	0.0350	0.0057	34%	37%

The results of this benchmark study show that the theoretical calculations employed in MATLAB achieve a high degree of corroboration for the lift coefficients of symmetrical biplanes and the drag coefficients of asymmetrical biplanes. It is shown that the primary source of error exists on the formulation of the trailing edge internal surfaces. This is likely because only one round of method of characteristics is employed, neglecting the effects of reflected waves downstream of the central apexes.

Very little difference is observed when comparing pressure contours between inviscid and viscous turbulent simulation results as shown in figure 5.8. This shows that the difference between drag calculated is largely due to viscous effects.

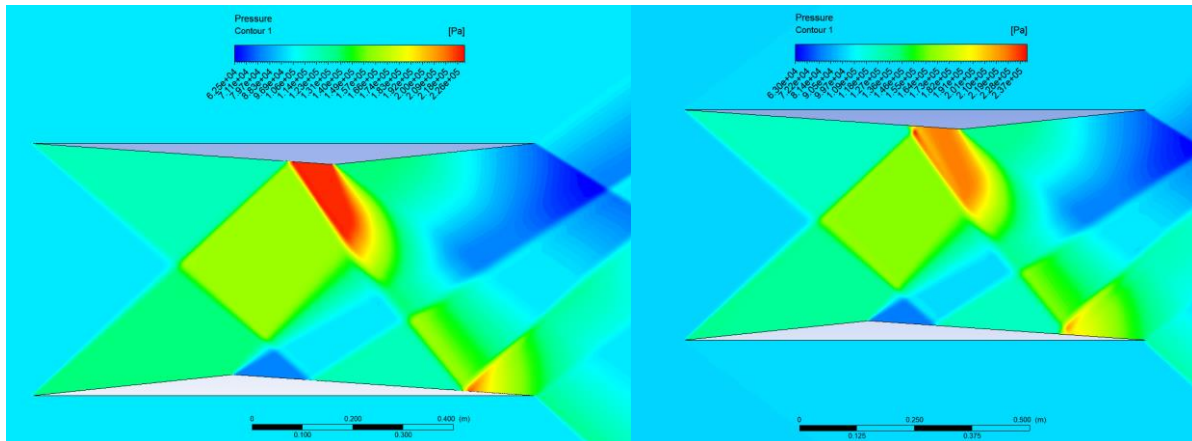


Figure 5.8 – Pressure contours of BL2 M1.7 inviscid vs viscous turbulent

5.2.2 Benchmark Study of the fanDensity Variable

A benchmark study of the effects of the variable fanDensity was conducted. As stated in Chapter 3, the variable fanDensity controls the number of Mach lines which comprise the expansion fans that form at the central apexes. This directly affects the number of characteristic lines that are imported into the method of characteristics section. Solutions become more accurate as fanDensity increases, however, computation time also increases exponentially. This benchmark study was again conducted for Baseline 1 and Baseline 2 at Mach 1.7 and Mach 2. The following graphs show the relationship between calculation time and the variable fanDensity plotted against the lift and drag coefficients for each case. In each case, convergence is achieved at a fanDensity value of approximately 20.

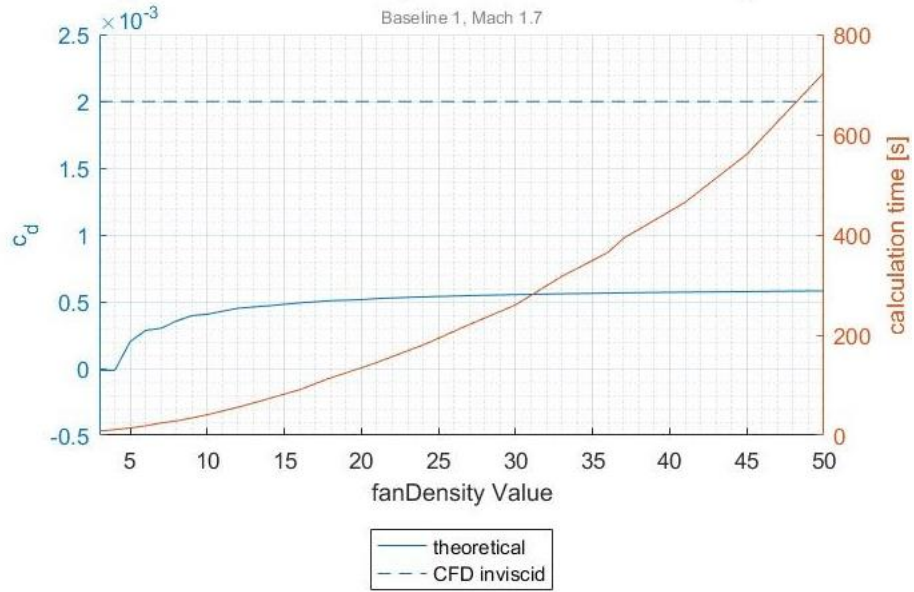


Figure 5.9 – Drag coefficient & computation time vs fanDensity values, baseline 1, Mach 1.7

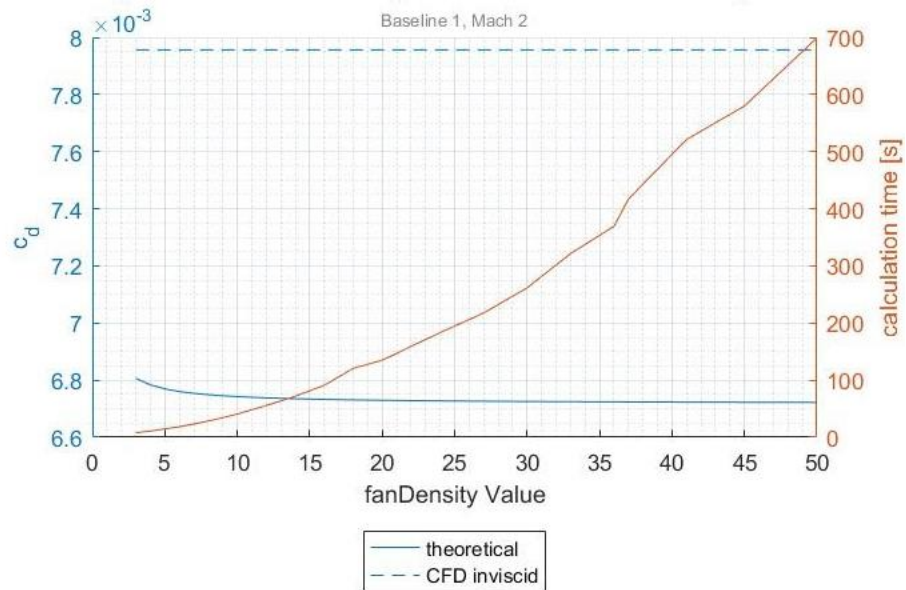


Figure 5.10 – Drag coefficient and computation time vs fanDensity values, baseline 1, Mach 2

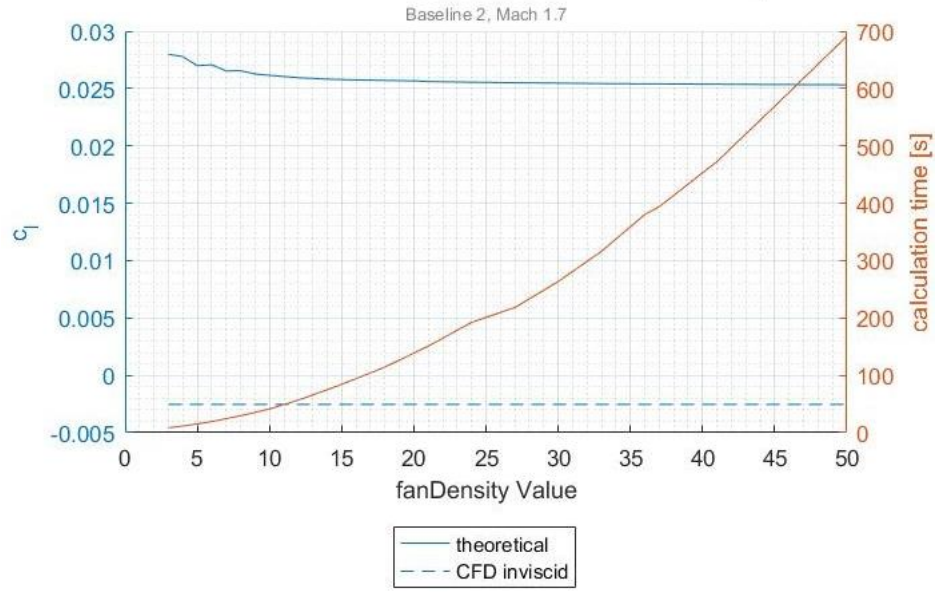


Figure 5.11 - Lift coefficient and computation time vs fanDensity values, baseline 2, Mach 1.7

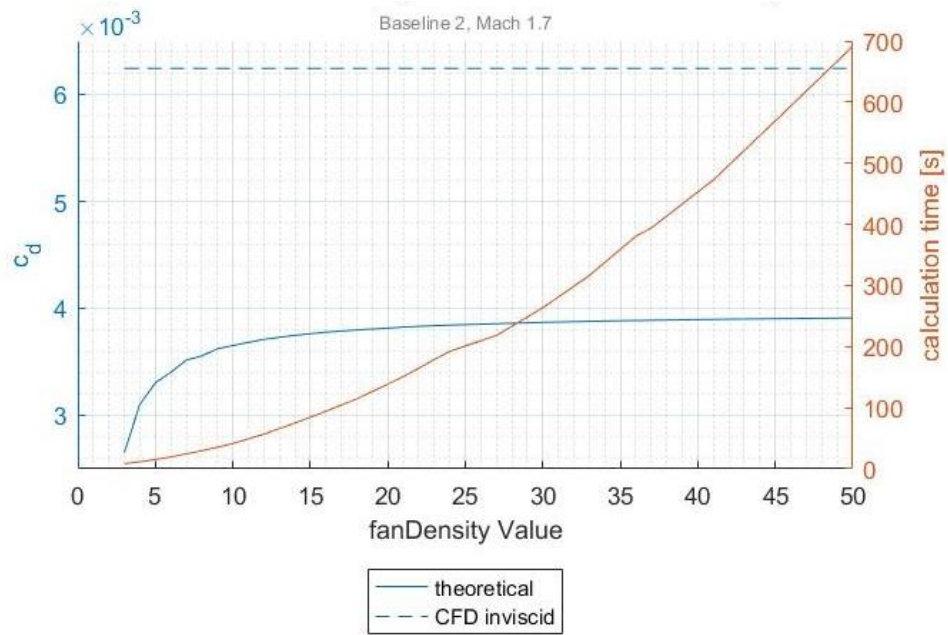


Figure 5.12 – Drag coefficient and computation time vs fanDensity values, baseline 2, Mach 1.7

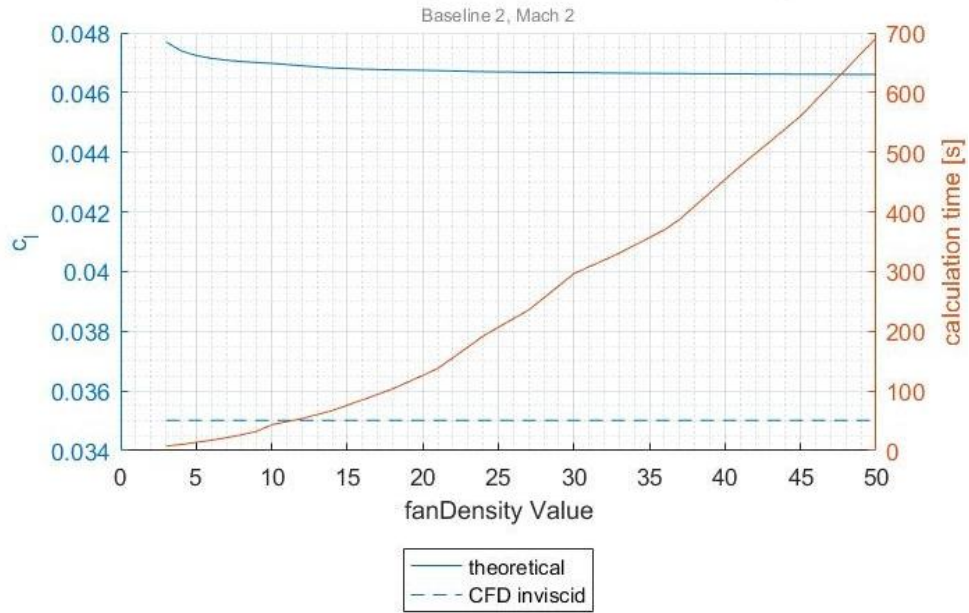


Figure 5. 13 – Drag coefficient and computation time vs fanDensity values, baseline 2, Mach 2

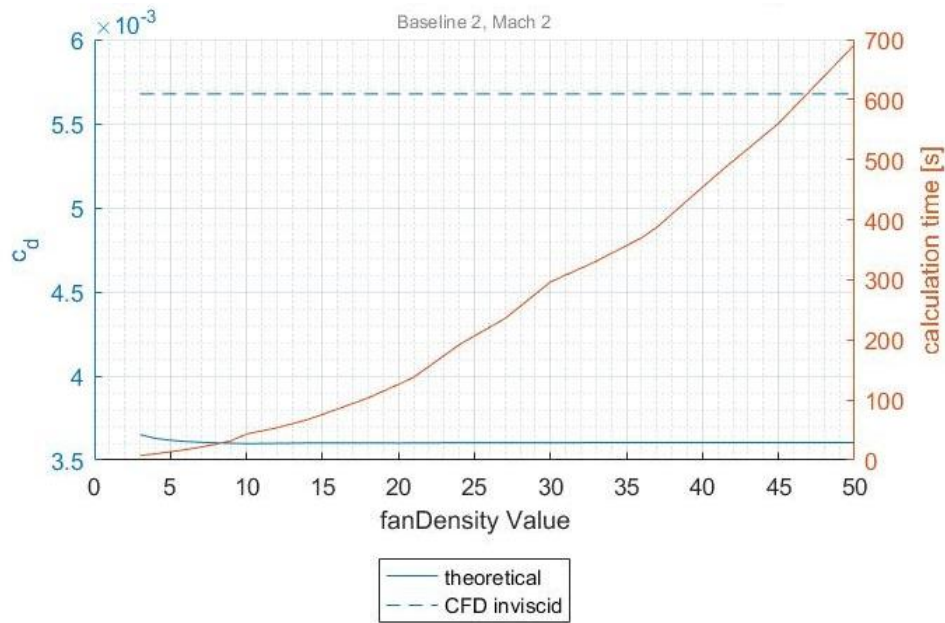


Figure 5. 14 – Lift coefficient and computation time vs fanDensity values baseline 2, Mach 2

Chapter 6 – Optimization of Supersonic Biplane

The Busemann biplane will be optimized with the ANSYS Fluent direct optimization platform. Airfoils will be kept at zero angle of attack. The design variables to be taken into consideration will be:

- LLA
- LTA
- ULA
- UTA
- LC
- UC
- VO
- HO

The theoretical calculator will be used to investigate the design space to determine appropriate limits.

6.1 Exploration of the Design Space using MATLAB

Moving forward, the MATLAB-based theoretical calculator can be used to perform a design space exploration determining the limits at which the given design will experience strong shocks or otherwise subsonic flow. The results shown in the benchmark studies indicate that the MATLAB-based theoretical calculator is not accurate enough to be used to find lift and drag coefficients. However, there is still a certain amount of utility to this method, in that no results can be achieved if flow is reduced to subsonic conditions. Multiple methods were employed -

- Symmetric body angles with:
 - varied chord lengths
 - varied vertical and horizontal offsets
- Asymmetric, fully random

These results show that it's still possible to maintain sonic flow with highly asymmetrical chord configurations.

6.1.1 Symmetric Body Angles with Varied Vertical and Horizontal Offsets

For the preliminary investigation, all body angles were set to the same randomly generated values between 4 and 15 degrees. Vertical offset was assigned random values between 0.35 and 0.65. Horizontal offset was assigned random values between -0.5 and 0.5. Lower and upper chord lengths were set to 1.

Figure 6.1 shows all the randomized designs that did not result in strong shocks or subsonic flow. Body angles had a maximum of 8.8 degrees. Designs that resulted in either single or double peak elimination at the apexes were rare beyond a body angle of 6 degrees. These results show that it's still possible to maintain sonic flow with highly asymmetrical chord configurations.

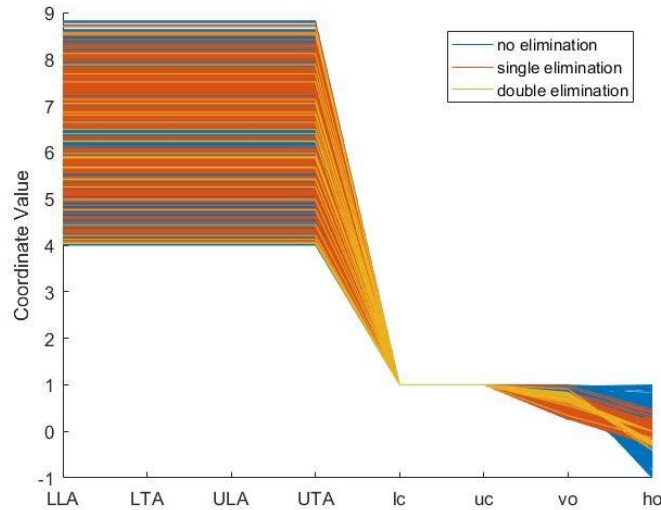


Figure 6. 1 - Parallel coordinate plot of symmetric body angles with varying vertical and horizontal offsets

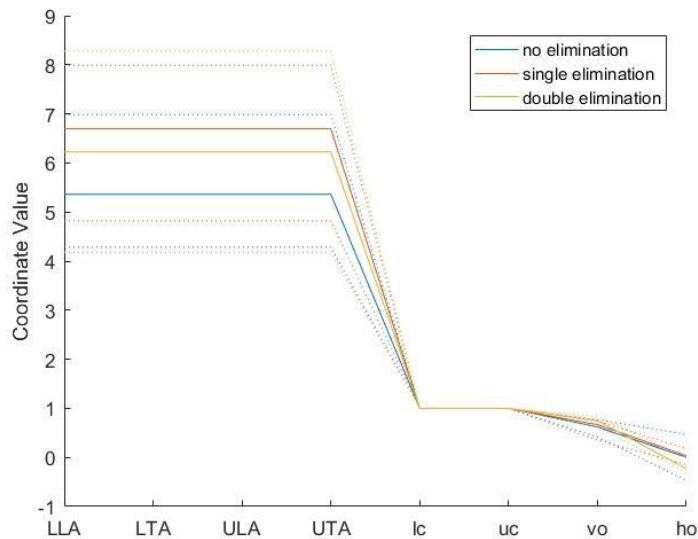


Figure 6. 2 - Quartile representation of fig. 6.1

Figures 6.3 and 6.4 show a 3D representation of the design space where body angles are on the A axis, providing a view of the shape of the design space.

- A clearly angled shape can be seen with designs that experience either single or double elimination at the extremes.
- Designs where body angles were greater than 6 primarily occurred when vertical offset was greater than 0.6, facilitating multiple opposite family shock interactions

- Designs with low vertical offset (less than 0.5) and low horizontal offset were difficult to achieve

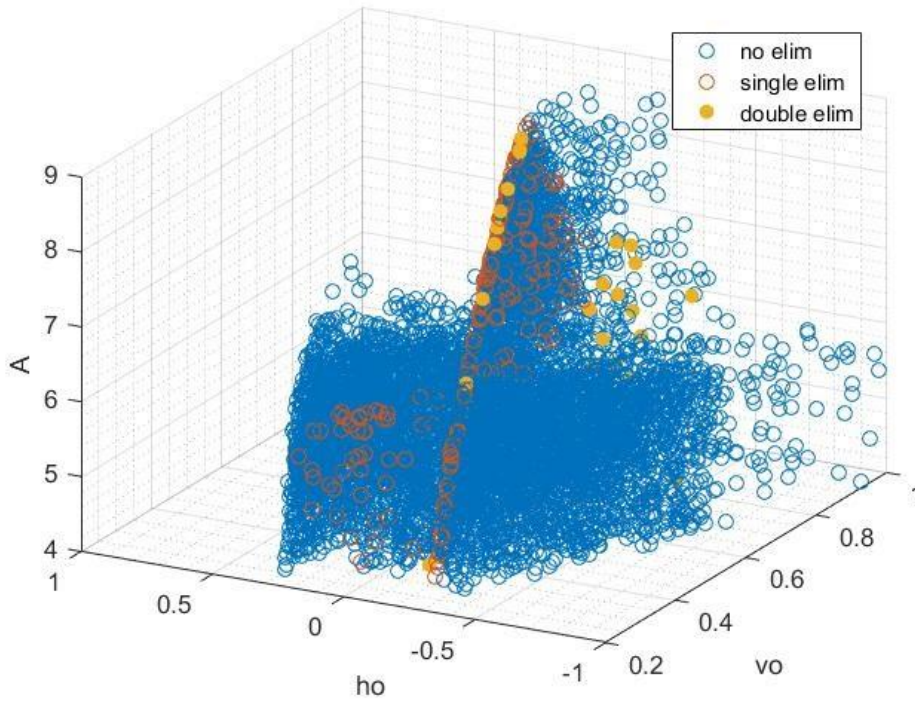


Figure 6. 3 - 3D scatter plot representation of fig. 6.1

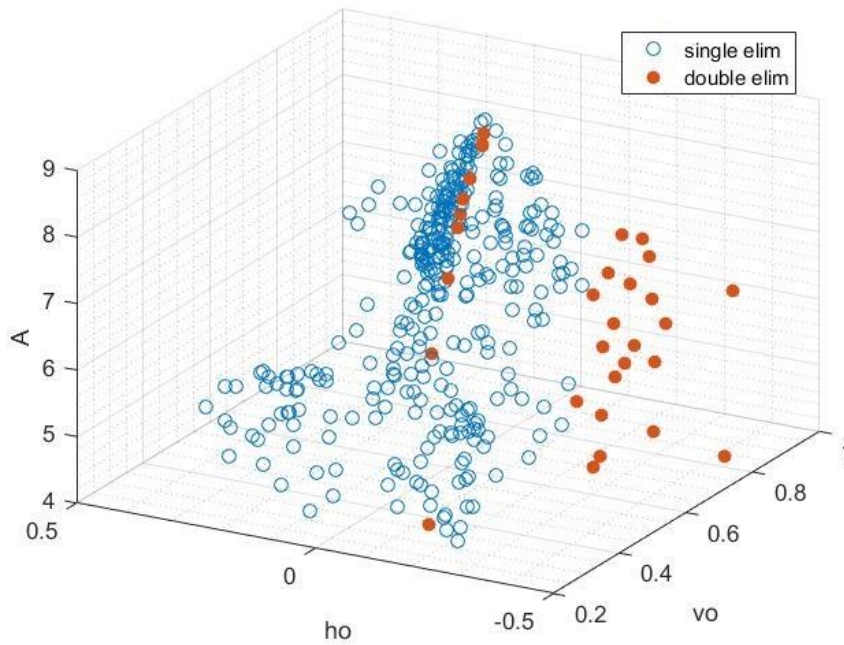


Figure 6. 4 - Single and double elimination points from fig. 6.1

6.1.2 Symmetric Body Angles with Varied Chord Lengths

For the preliminary investigation, all body angles were set to the same randomly generated values between 4 and 15 degrees. Lower and upper chord lengths were assigned randomly between 0.5 and 2 meters. Vertical and horizontal offsets were set to the Baseline 1 values of 0.5 and 0.0 respectively.

Figure 6.1 shows all the randomized designs that did not result in strong shocks or subsonic flow. Body angles had a maximum of 8.8 degrees. Designs that resulted in either single or double peak elimination at the apexes were rare beyond a body angle of 6 degrees. These results show that it's still possible to maintain sonic flow with highly asymmetrical chord configurations.

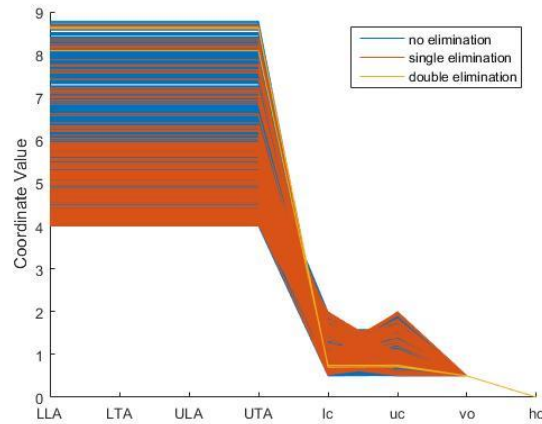


Figure 6. 5 – Parallel coordinate plot of symmetric body angles with varying chord lengths

Figure 6.6, the quartile representation of the same data, shows the median (solid line), 25% (dashed) and 75% (dashed) quartile values, which were helpful to visualize better designs.

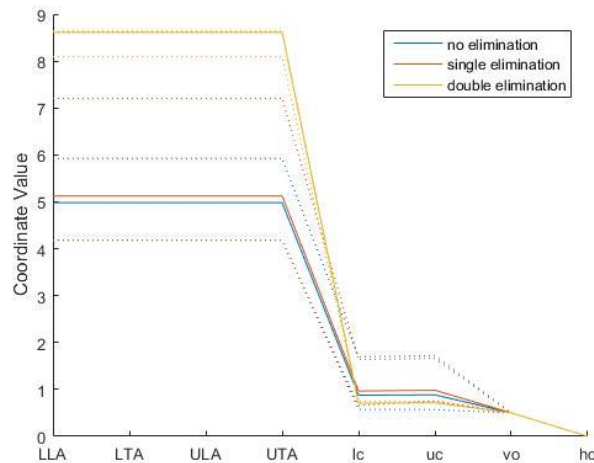


Figure 6. 6 – Quartile representation of fig. 6.5

Figures 6.7 and 6.8 show a 3D representation of the design space where body angles are on the A axis. This provides a view of the shape of the design space.

- A clearly angled shape can be seen with designs that experience either single or double elimination at the extremes.
- Additionally, it shows that designs where the sum of the chord lengths greater than 2 were difficult to achieve.
- Designs where body angles were greater than 6 primarily occurred when the sum of the chord lengths was less than 2.

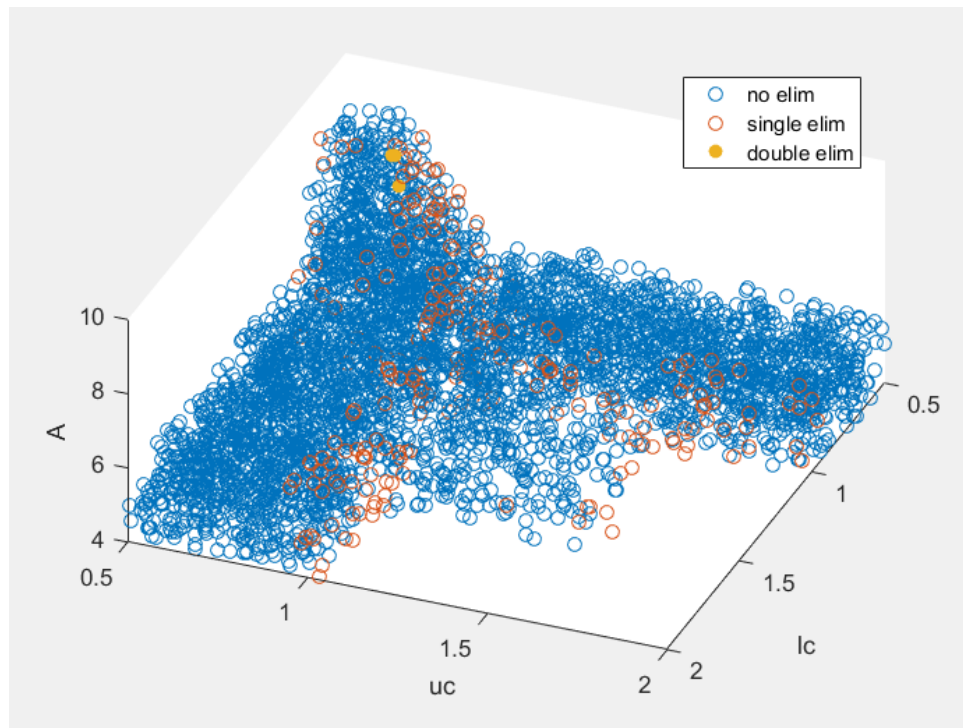


Figure 6. 7 – 3D scatter plot representation of fig. 6.5

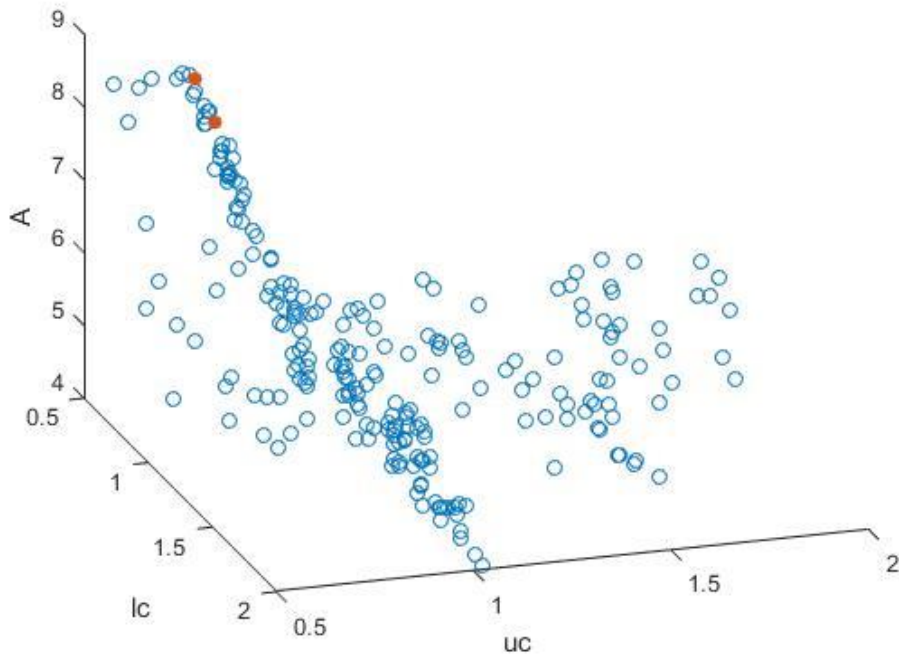


Figure 6. 8 – Single and double elimination points from fig. 6.5

6.1.3 Asymmetric Body Angles, Fully Random Chord Lengths and Offsets

For the preliminary investigation, all body angles were set to the same randomly generated values between 4 and 18 degrees. Lower and upper chord lengths were assigned randomly between 0.5 and 2 meters. Vertical offset was assigned random values between 0.35 and 0.65. Horizontal offset was assigned random values between -0.5 and 0.5.

Figure 6.9 shows all the randomized designs that did not result in strong shocks or subsonic flow. Designs that resulted in either single or double peak elimination at the apexes occurred primarily when leading edge body angles were low (below 6 degrees). These results show that it is still possible to maintain sonic flow with highly asymmetrical configurations.

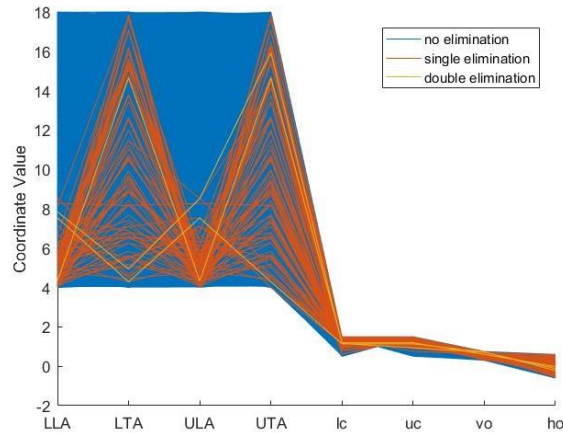


Figure 6. 9 - Parallel coordinate plot of asymmetric body angles with varying vertical and horizontal offsets

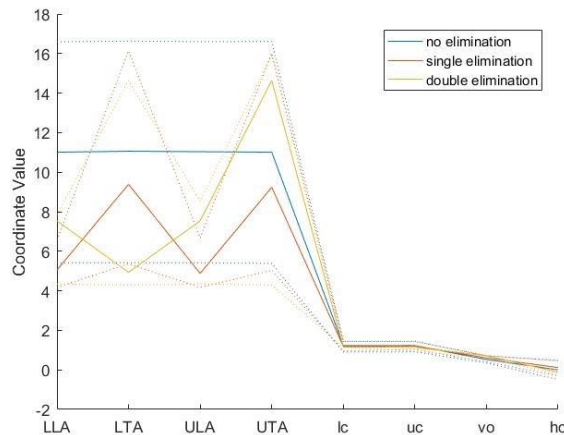


Figure 6. 10 – Quartile representation of fig. 6.9

6.2 ANSYS Direct Optimization

The ANSYS direction optimization platform was used to optimize the parameters of the Busemann biplane. The optimization scheme employed was the adaptive multi-objective genetic algorithm. This optimization scheme is an iterative method that combines standard multi-objective genetic algorithms and Kriging response surfaces. [12]

The design space employed involved 8 variables:

- LLA
- LTA
- ULA
- UTA
- LC
- UC
- HO
- VO

6.2.1 Symmetric Body Angles with Varied Vertical Offset

Table 6.1 shows the range of input parameters. These values were estimated from the fully asymmetric investigation performed in MATLAB as described in section 6.1. The values for LLA and ULA are set equal to the value of LA. The same is true for the values of UTA and LTA which were set to the value of TA. This investigation was for the purpose of refining allowable body angle values.

Table 6. 1 – Range of input parameters (VO only)

Table of Schematic D2: Optimization				
	A	B	C	D
1	[- Input Parameters			
2	Name	Lower Bound	Upper Bound	
3	P55 - VO (m)	0.4	0.6	
4	P59 - LA (degree)	4	8	
5	P60 - TA (degree)	4	16	
6	[+ Parameter Relationships			
*	<i>New Parameter Relationship</i>	<i>New Expression</i>	<=	<i>New Expression</i>

Table 6.2 outlines the results of the direct optimization scheme employed. These are the design candidate points. Of the 84 potential designs generated and tested, three are recommended by ANSYS for further analysis. All three candidate design points had a drag coefficient comparable to the baseline. Although the x's indicate the candidate design points did not converge to a stable design during the 3 generations allowed, the coefficients of the final candidate points are accurate.

Table 6. 2 – Design candidate points (VO)

7	[- Candidate Points			
8		Candidate Point 1	Candidate Point 2	Candidate Point 3
9	P55 - VO (m)	0.50429	0.40588	0.50429
10	P59 - LA (degree)	4.0272	4.0429	4.102
11	P60 - TA (degree)	4.0685	4.0857	4.6783
12	P65 - cd-op	✖✖ 0.0025262	✖✖ 0.0025373	✖✖ 0.002901

6.2.2 Symmetric Body Angles with Varied Vertical and Horizontal Offsets

Table 6.3 shows the range of input parameters. These values were estimated from the fully asymmetric investigation performed in MATLAB as described in section 6.1. The values for LLA and ULA are set equal to the value of LA. The same is true for the values of UTA and LTA which were set to the value of TA. This investigation was for the purpose of further refining allowable body angle values.

Table 6.3 – Range of input parameters (VO, HO)

Input Parameters			
Name	Lower Bound	Upper Bound	
P53 - HO (m)	2.5	3.5	
P55 - VO (m)	0.375	0.6	
P59 - LA (degree)	4	8	
P60 - TA (degree)	4	16	

Table 6.4 outlines the results of the direct optimization scheme employed. Out of the 175 potential designs generated and tested, three are recommended by ANSYS for further analysis. These design candidate points experience higher drag than baseline 1. This simulation was allowed to run for five generations and as such, reached a higher level of convergence in the genetic algorithm.

Table 6.4 - Design candidate points (VO, HO)

	Candidate Point 1	Candidate Point 2	Candidate Point 3
P53 - HO (m)	3.2273	3.2327	3.2329
P55 - VO (m)	0.56806	0.56806	0.56067
P59 - LA (degree)	4.026	4.0116	4.034
P60 - TA (degree)	4.1772	4.2983	4.4903
P57 - cd-op	✘ 0.0038236	✘ 0.0039593	✘✘ 0.0040455

6.2.3 Asymmetric Body Angles, Fully Random Chord Lengths and Offsets

Table 6.5 shows the range of all input parameters. These values were estimated from the fully asymmetric investigation performed in MATLAB as described in section 6.1. Parameter relationships ensured that the sum of the chord lengths was greater than 1.9, and the difference between them was no greater than 0.4. The reason for the limitation on the difference was to compensate for design point failures in ANSYS. Per the results shown in section 6.2.1 and 6.2.2, body angle upper bounds were decreased to 7.5 degrees to reduce the impact of strong shocks.

Table 6. 5 – Range of input parameters – all parameters

Table of Schematic H2: Optimization				
	A	B	C	D
1	[-] Input Parameters			
2	Name	Lower Bound	Upper Bound	
3	P53 - HO (m)	2.5	3.5	
4	P55 - VO (m)	0.45	0.6	
5	P61 - UC (m)	0.75	1.25	
6	P68 - LLA (degree)	4	6	
7	P69 - ULA (degree)	4	6	
8	P70 - UTA (degree)	4	7.5	
9	P71 - LTA (degree)	4	7.5	
10	P72 - LC (m)	0.75	1.25	
11	[+] Parameter Relationships			
13	(P61-P72) <= .4 [m]	(P61-P72)	<=	[v] .4 [m]
14	(P72-P61) <= .4 [m]	(P72-P61)	<=	[v] .4 [m]
15	(P72+P61) >= 1.9 [m]	(P72+P61)	>=	[v] 1.9 [m]

Table 6.6 outlines the results of the direct optimization scheme employed. Of the 137 potential designs generated and tested, three are recommended by ANSYS for further analysis. These design candidate points experience higher drag than baseline 1. This simulation was allowed to run for five generations; however, design point convergence of the genetic algorithm was lower than results seen in section 6.2.2 upon completion.

Table 6. 6 - Design candidate points – all parameters

7	[-] Candidate Points			
8		Candidate Point 1	Candidate Point 2	Candidate Point 3
9	P53 - HO (m)	2.8404	2.9764	2.979
10	P55 - VO (m)	0.46686	0.54258	0.45597
11	P61 - UC (m)	1.0795	1.0955	1.0787
12	P68 - LLA (degree)	4.5963	5.5597	4.1732
13	P69 - ULA (degree)	4.038	4.7311	4.7354
14	P70 - UTA (degree)	4.4709	4.8518	4.8399
15	P71 - LTA (degree)	4.3836	4.404	4.3895
16	P72 - LC (m)	0.9016	1.1131	1.0815
17	P65 - cd-op	✖ ✖✖ 0.0034156	✖ ✖✖ 0.0035126	✖ ✖✖ 0.0035363

Chapter 7 – Conclusion

The original premise of this project was to further investigate the optimization methods employed for the Busemann biplane for its potential to generate lift at supersonic speeds without the typically associated sonic boom. Past researchers have found impressive results in optimizing the design using modern techniques and showed that, potentially, the issues of flow choking and flow hysteresis may be mitigated or eliminated.

Most of the past research conducted had been limited in scope, performing minor surface curvature optimization, altering the relative position of the two airfoils or implementing control surfaces. This paper has shown that there is the potential to optimize the concept of a supersonic biplane by varying numerous design parameters at once.

Additionally, the use of MATLAB was introduced as a method to refine the design space, thereby reducing analysis time.

As a result of all experiments conducted, the following conclusions can be reached:

- The lift and drag coefficients of the Busemann biplane are always highly dependent on the internal shock wave interactions.
- It is not enough for a general theoretical calculator of Busemann-type biplanes to consider only the first set of wave interactions beyond the central apexes.
- It is possible to achieve double apex elimination with highly irregular designs.
- While it is possible to achieve lift and drag coefficients comparable to the baseline with a highly irregular design, it is extremely difficult and rare due to the complex nature of the shock wave interactions.
- The results from the NACA 1316 report could not be substantiated through ANSYS.

7.1 Future Work

There is utility in developing a theoretical solver for Busemann-type biplanes which would facilitate faster calculation of the lift and drag coefficients. This solver would need to consider all reflected waves downstream of the central apexes.

Additionally, further utilization of genetic algorithms is recommended to refine the design of Busemann-type biplanes.

Asymmetric simulations would require larger initial sample set size in the ANSYS set up.

References

- [1] Moeckel, W.E., “Theoretical Aerodynamic Coefficients of Two-Dimensional Supersonic Biplane,” NACA T.N. No. 1316, June 1947.
- [2] Patidar, V.K., Yadav, R. and Joshi, S., “Numerical Investigation of the Effect of Stagger on the Aerodynamic Characteristics of Busemann Biplane,” *Aerospace Science and Technology*, Vol. 55, Aug. 2016, pp. 252–263.
- [3] Ma, B., Wang, G., Wu, J., and Ye, Z., “Avoiding Choked Flow and Flow Hysteresis of Busemann Biplane by Stagger Approach,” *Journal of Aircraft*, Vol. 57, Jan. 2020, pp. 440–455.
- [4] Daigo, M., “Aerodynamic Design of Three-Dimensional Biplane Wings for Low Wave- Drag Supersonic Flight,” *ICAS 2008: 26th Congress of the International Council of the Aeronautical Sciences including the 8th AIAA Aviation Technology, Integration, and Operations (ATIO) Conference*, Anchorage, Alaska, USA, 14-19 September 2008.
- [5] Yamashita, H., Yonezawa, M., Obayashi, S., and Kusunose, K., “A Study of Busemann-Type Biplane for Avoiding Choked Flow,” *45th AIAA Aerospace Sciences Meeting and Exhibit*, January 2007.
- [6] Daigo, M., Kusunose, K., Matsushima, K., and Matsuzawa, T., “25th International Congress of the Aeronautical Sciences,” Numerical Design And Assessment Of A Biplane As Future Supersonic Transport ----- Revisiting Busemann’s Biplane -----,” Hamburg, Germany, 2006.
- [7] Zhai, J., Zhang, C.A., Wang, F.M., and Zhang, W.W., “Design of a New Supersonic Biplane,” *Acta Astronautica*, Vol. 175, October 2020, pp. 216–233.
- [8] Tian, Yi., “Shape Optimization of Busemann-type Biplane Airfoil for Drag Reduction under Non-lifting and Lifting Conditions Using Genetic Algorithms,” Engineering and Applied Science Theses and Dissertations, Washington University, St. Louis, Missouri, August 2015
- [9] Kusunose, K., Matsushima, K., and Maruyama, D., “Supersonic biplane—A Review,” *Progress in Aerospace Sciences*, Vol. 47, Nov. 2010, pp. 53–87.
- [10] Anderson, J. D., *Fundamentals of Aerodynamics*, McGraw-Hill, New York, 2011.
- [11] Anderson, J.D., *Modern Compressible Flow: with Historical Perspective*, McGraw Hill, Boston, Mass., 2003.
- [12] Module 5 Optimization, *Introduction to ANSYS DesignXplorer*, May 2016, pp. 10-13.